MIT JOINT PROGRAM
SCIENCE · POLICY
GLOBAL CHANGE

A Large Ensemble Global Dataset for Climate Impact Assessments

Xiang Gao, Andrei Sokolov and C. Adam Schlosser

MIT Joint Program on the Science and Policy of Global Change combines cutting-edge scientific research with independent policy analysis to provide a solid foundation for the public and private decisions needed to mitigate and adapt to unavoidable global environmental changes. Being data-driven, the Joint Program uses extensive Earth system and economic data and models to produce quantitative analysis and predictions of the risks of climate change and the challenges of limiting human influence on the environment—essential knowledge for the international dialogue toward a global response to climate change.

To this end, the Joint Program brings together an interdisciplinary group from two established MIT research centers: the **Center for Global Change Science (CGCS)** and the **Center for Energy and Environmental Policy Research (CEEPR)**. These two centers—along with collaborators from the Marine Biology Laboratory (MBL) at

Woods Hole and short- and long-term visitors—provide the united vision needed to solve global challenges.

At the heart of much of the program's work lies MIT's Integrated Global System Model. Through this integrated model, the program seeks to discover new interactions among natural and human climate system components; objectively assess uncertainty in economic and climate projections; critically and quantitatively analyze environmental management and policy proposals; understand complex connections among the many forces that will shape our future; and improve methods to model, monitor and verify greenhouse gas emissions and climatic impacts.

This report is intended to communicate research results and improve public understanding of global environment and energy challenges, thereby contributing to informed debate about climate change and the economic and social implications of policy alternatives.

*—**Ronald G. Prinn**,*
Joint Program Director

A Large Ensemble Global Dataset for Climate Impact Assessments

Xiang Gao[1], Andrei Sokolov[1], and C. Adam Schlosser[1]

Abstract: We present a self-consistent, large ensemble, high-resolution global dataset of long-term future climate developed by integrating a spatial disaggregation (SD) pattern-scaling technique and a bias-correction (BC) delta method. The delta method adds the anomalies or deltas (future climate trends) onto a historical, detrended climate that is based on the third phase of the Global Soil Wetness Project (GSWP3). The anomalies or deltas are derived by spatially disaggregating zonal climate projections from the MIT Integrated Global System Modeling (IGSM) framework based on regional hydroclimate change patterns from the 18 Coupled Model Intercomparison Project Phase 6 (CMIP6) climate models. Four emission scenarios are considered to represent the existing energy and environmental policies and commitments of potential future pathways, namely, Reference, Paris Forever, Paris 2°C and Paris 1.5°C. For each emission scenario, a distribution of plausible trajectories is provided by a 50-member ensemble to represent the uncertainty in the Earth system (e.g., the climate sensitivity, rate of heat uptake by the ocean, uncertainty in carbon cycle), allowing for constructing a 900-member ensemble of regional climate outcomes. This global dataset contains nine key meteorological variables on a monthly scale from 2021 to 2100 at a spatial resolution of 0.5°x 0.5°, including precipitation, air temperature (mean, minimum and maximum), near-surface wind speed, shortwave and longwave radiation, specific humidity, and relative humidity. Quantitative assessments clearly indicate the ability of the dataset to represent the expected large-scale climate features across various regions of the globe. This large-ensemble, high-resolution dataset can be used for assessing impacts of climate change from a risk-based perspective across different applications, including hydropower, water resources, wind power resources to name a few.

1. Introduction

Global climate model (GCM) simulations of the past, current, and future climate have become readily available through the different phases of the Coupled Model Intercomparison Project (CMIP). Over the past several decades, the CMIP data archive has served as a foundational element of climate science and for supporting decision and policy-makers communities. The recent sixth phase of CMIP (CMIP6, Eyring *et al.*, 2016) has expanded the breadth of the coordinated climate model experiments considerably with more than 70 participating models of a wide variety from more than 30 participating model groups worldwide.

The Scenario Model Intercomparison Project (ScenarioMIP) in CMIP6 provides the main set of future climate projections based on alternative scenarios directly relevant to societal concerns for climate change mitigation, adaptation, or impacts (O'Neill *et al.*, 2016). These climate projections are driven by a set of emissions and land use scenarios (Riahi *et al.*, 2016) produced with integrated assessment models (IAMs) based on future pathways of societal development, the Shared Socioeconomic Pathways (SSPs), and related to the forcing levels of the Representative Concentration Pathways (RCPs). Compared to CMIP5, CMIP6 RCPs fill critical gaps for intermediate forcing levels (for example, short-lived species and land use) and the full set of SSPs-RCPs combinations spans a larger range of outcomes. However, these multi-model climate projections under a matrix of possible integrated scenarios may not adequately represent the desired risk-based assessment of climate change impacts and climate policy benefits due to several issues described below. First, there is a lack of the consistency in socioeconomic and environmental factors and such consistency is highly relevant for assessing climate impacts and climate policy benefits. These model projections have been driven with exogenous climate forcing that is disconnected from consistent socioeconomic pathways, thus lacking the interactions between natural processes and human activities. These inconsistencies arise mainly because the developers and the users of these socioeconomic scenarios come from different research groups and disciplinary communities. For example, even with a common land use scenario implemented, the different Earth system models can have different interpretations of land use classes, making the resulting differences in the carbon cycle and land use forcing difficult to interpret. Further, each of the integrated scenarios was produced by a different group and their projections of future air pollutant emissions are not consistent with one another, which can contaminate the analysis of climate policy benefits. Second, the coarse resolutions (70-400 km) and inherent biases of climate model outputs are not suitable for local-scale climate impact studies, particularly when they are used as drivers into impact models (i.e., hydrological models, crop

models, biodiversity evaluation, etc.). Third, the ensemble of climate projections from the participating climate modes falls short of providing quantitative insights on 'risk' or the probability of variables of interest.

We address these issues by developing a self-consistent, large ensemble, high-resolution, bias-corrected global dataset of future climates for a set of possible 21st century scenarios. We employ the MIT Integrated Global System Modeling (IGSM) framework, which consists of the MIT Earth System Model (MESM) of intermediate complexity and the Economic Projections and Policy Analysis model (EPPA) (Sokolov *et al.*, 2018). The EPPA characterizes detailed economic activities to track inter-sectoral and inter-regional links, while the MESM represents key physical, chemical, and biological components of the Earth system that are impacted by human activity. Such integrated framework ensures consistent treatment of interactions among population growth, economic development, energy and land system changes and physical climate responses, which can provide improved assessments of climate impacts across multiple sectors (Monier *et al.*, 2018). The MESM contains a two-dimensional (zonally averaged) atmospheric model with interactive chemistry coupled to the zonally averaged version of Global Land System model and an anomaly-diffusing ocean model. This architecture allows for conducting a large ensemble of climate simulations for robust uncertainty analyses at significantly less computational cost than state-of-the-art climate models. In addition, we apply a combined spatial disaggregation (SD)—bias correction (BC) method with SD for achieving the high resolution and BC for correcting the biases inherent in the MESM future climate projections.

The paper is organized as follows. Section 2 presents the data sets used in this study. Section 3 describes the employed SD-DC method. A quantitative evaluation of an ensemble of future climate projections is presented in section 4 followed by a summary in section 5.

2. Data

2.1 Historical Meteorology

We utilize the historical meteorological dataset from the third phase of the Global Soil Wetness Project (GSWP3, http://hydro.iis.u-tokyo.ac.jp/GSWP3/) as the baseline climate. It is a 3-hourly 0.5° global forcing product (1901–2014) based on the 20th Century Reanalysis version 2 (Compo *et al.*, 2011). The reanalysis was dynamically downscaled to 0.5° resolution based on the Global Spectral Model using a spectral nudging technique (Yoshimura and Kanamitsu, 2008). Bias corrections based on observations were made for temperature, precipitation, and longwave radiation, and shortwave radiation using CRU TS v3.21 (Climate Research Unit, Jones and Harris, 2013), GPCCv7

(Global Precipitation Climatology Centre, Schneider *et al.*, 2014), and Surface Radiation Budget data sets, respectively. A wind-induced undercatch correction was also applied.

The meteorological variables considered in this study include precipitation, air temperature (mean, minimum and maximum), near-surface wind speed, shortwave and longwave radiation, specific humidity, and relative humidity. Minimum and maximum air temperature as well as relative humidity are not provided in the GSWP3 data, but derived as follows. Minimum and Maximum air temperature are calculated as the monthly means of the minimum and maximum daily air temperature across the 8 3-hourly time steps, respectively. Relatively humidity is derived from surface air temperature (T_{air}), surface air pressure (Psf), and specific humidity (Q_{air}) at a 3-hourly time step as in equation (1) and averaged into the monthly values.

$$e_s = 6.112 * e^{\frac{17.67*T_{air}}{T_{air}+243.5}}, \ e = Q_{air} * \frac{Psf}{0.378*Q_{air}+0.622}, \ rh = 100 * \frac{e}{e_s} \quad (1)$$

Where e and e_s are vapor pressure and saturated vapor pressure, respectively. rh is the relative humidity in percent.

2.2 CMIP6 Model Simulations

The CMIP has become one of the foundational elements of climate science by distributing global climate model simulations of the past, current, and future climate. The CMIP6 includes more than 70 participating models of a wide variety developed at research institutes across the international scientific community. For the SD pattern-scaling procedure used in the construction of our large-ensemble future projections at the 0.5° resolution, we draw the simulations of the participating models from the 1pctCO$_2$ experiment in which the concentration of atmospheric CO$_2$ increases gradually at a rate of 1% per year from the global annual mean 1850 value until quadrupling. It serves as a consistent and useful benchmark for analyzing model transient climate response (TCR) to cumulative carbon emissions (TCRE). Multiple variations of model outputs may be available from a model family with different configurations (e.g., different spatial resolutions or components). In that case, only one sibling model is selected to represent the family. The precedence for selection is (highest to lowest): 1) all the key meteorological variables of our interest are archived, including precipitation, air temperature (mean, minimum and maximum), near-surface wind speed, shortwave and longwave radiation, specific humidity, and relative humidity; 2) an Earth System Model (ESM) is chosen whenever available; and 3) higher spatial resolution is desired. This resulted in 18 climate models that participated in the CMIP6 1pctCO$_2$ experiment (**Table 1**). Their corresponding monthly outputs are then obtained for the pattern-scaling method (Section 3.2).

2.3 IGSM Future Climate Projections

A self-consistent, large ensemble of zonal future climate projections is constructed with the MIT IGSM. We focus on four policy scenarios that were developed to span a range of possible global actions to abate greenhouse gas

Table 1: List of CMIP6 models used in our study to construct the pattern-scaling kernels of climate change response.

Model Name	Resolution	Institution
ACCESS-ESM1-5	1.875° × 1.25°	Australian Commonwealth Scientific and Industrial Research Organization
AWI-ESM-1-1-LR	1.875° × 1.875°	German Alfred Wegener Institute
BCC-CSM2-MR	1.125° × 1.125°	Beijing Climate Center
CanESM5	2.8125° × 2.8125°	Canadian Centre for Climate Modelling and Analysis
CMCC-ESM2	1.25° × 0.9375°	Centro Euro-Mediterraneo Cambiamenti Climatici
CNRM-ESM2-1	1.40625° × 1.40625°	Centre National de Recherches Meteorologiques
EC-Earth3-Veg	0.703125° × 703125°	EC-Earth-Consortium
FGOALS-g3	2.0° × 2.25°	Chinese Academy of Sciences
FIO-ESM-2-0	1.25° × 0.9375°	Qingdao National Laboratory for Marine Science and Technology
GISS-E2-2-G	2.5° × 2.0°	Goddard Institute for Space Studies
HadGEM3-GC31-MM	0.83° × 0.56°	Met Office Hadley Centre
INM-CM5-0	2.0° × 1.5°	Russian Academy of Science
IPSL-CM6A-LR	2.5° × 1.26°	Institut Pierre Simon Laplace
MIROC-ES2L	2.8125° × 2.8125°	Japan Agency for Marine-Earth Science and Technology
MPI-ESM1-2-HR	0.9375° × 0.9375°	Max Planck Institute for Meteorology
MRI-ESM2-0	1.125° × 1.125°	Japan Meteorological Research Institute
SAM0-UNICON	1.25° × 0.9375°	Seoul National University
UKESM1-0-LL	1.875° × 1.25°	Met Office Hadley Centre

emissions over the coming century, specifically **Reference (REF)**, **Paris Forever (PF)**, **Paris 2°C (P2C)**, and **Paris 1.5°C (P1p5C)**. The **REF** scenario implements no explicit climate mitigation policy (no specific greenhouse gas emissions target) anywhere in the world for the sake of abating climate change, except for some energy policies such as fuel economy standards, renewable electricity requirements, the gradual phase-out of old coal power plants, reduced use of exhaustible resources, and conventional pollutants reduction. The REF serves as a baseline scenario and represents the upper bound of climate change risks. The **PF** scenario assumes that all Paris Agreement Nationally Determined Contributions (NDCs) are implemented through the year 2030 and maintained in perpetuity after that. While our PF scenario represents an unprecedented global commitment to limit greenhouse gas emissions, it neither stabilizes climate nor limits climate change. **P2C** and **P1p5C** scenarios extend from the Paris Agreement's NDCs and align with its long-term goals. These two scenarios aim to limit and stabilize human-induced global climate warming to 2°C and 1.5°C, respectively, by the end of this century. Variations in mitigation policies lead to the uncertainty in patterns of resource and energy use, technology choices, and drag on overall economic growth, with additional uncertainty arising from the global climate response represented in the MESM (Sokolov *et al.*, 2018). These co-evolving uncertainties result in an overall probability of achieving the target at 50% for both P2C and P1p5C scenarios. Detailed description of emission scenarios is given in Paltsev *et al.* (2021).

For each of four policy scenarios, a 50-member ensemble of MESM simulations is conducted to provide a range of Earth systems' response to natural and anthropogenic drivers. This 50-member ensemble replicates well the surface air temperature distribution from the 400-member ensemble simulations presented in Paltsev *et al.* (2021, not shown). In both cases climate parameters were sampled from 3-dimentional probability distribution described by Libardoni *et al.* (2018). These scenarios result in distinct pathways and distributions of global averaged changes in human forcing and climate variables (**Figures 1 and 2**). In comparison with the CMIP5 RCP scenarios, the IGSM REF scenario presents weaker radiative forcing than its RCP counterpart (RCP8.5), while the more aggressive climate-based targets (P2C and P1p5C) fall between RCP4.5 and RCP2.6 scenarios. The PF scenario characterizes stronger radiative forcing than the RCP6.0 scenario. The impact of the aggressive mitigation policies on alleviating or eliminating the warming risk is immediately evident, with a majority of the distributions of global averaged annual surface-air temperature (SAT) trends in P2C and P1p5C scenarios falling outside that of the REF scenario in the latter half of the 21st century (Figure 2). Despite a notable shift toward lower warming risk, considerable overlap persists till the end of the century between the SAT trends distributions of the PF scenario and those of the REF scenario.

2.4 Regions

We adopt 21 regions used in Giorgi and Francisco (2000) to evaluate the regional-scale performances of our dataset.
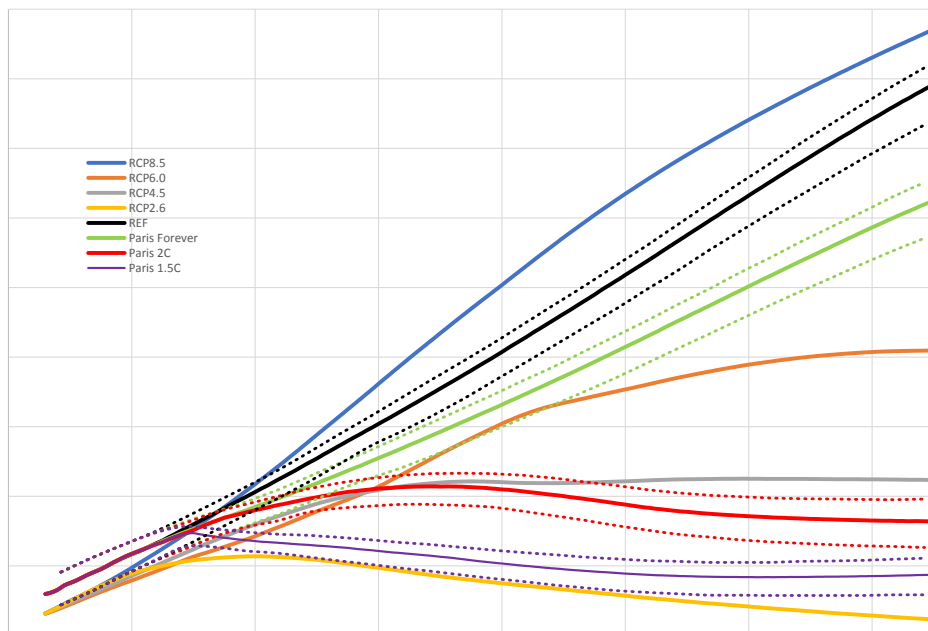

Figure 1. Total radiative forcing (relative to 1860, W/m2) from the four MIT IGSM policy scenarios used in this study, compared to that from the Representative Concentration Pathway (RCP) experiments in CMIP5. The dotted lines indicate 5% and 95% percentiles, respectively.
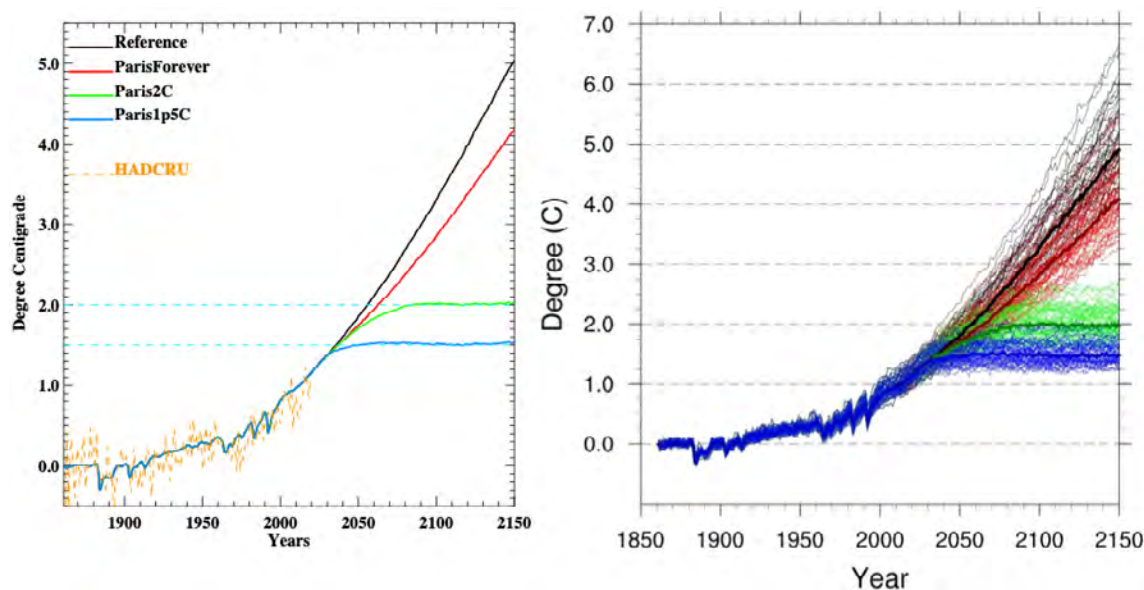
Figure 2. Global averaged annual surface-air temperature trends for the four MIT IGSM policy scenarios. The left panel presents the median trajectories of the 50-member IGSM ensemble, while the right panel provides the trajectories from all ensemble members. Trends in temperature are calculated relative to the 1861-1880 mean.

The detailed information of 21 regions is listed in **Table 2**. These regions represent different climatic regimes and physiographic settings, and are defined to approximately cover all land areas in the World with the size of each region varying in the range of a few thousand to several thousand km in each direction (Giorgi and Francisco, 2000). The evaluation is conducted on the regional averages of seasonal means across the entire time period for each variable. The relevant ensemble statistics (minimum, median, and maximum) are derived based on the regional averages of seasonal means of each ensemble member.

3. Methods

We employ an integrated SD-BC method to develop a long-term (2021-2100), large ensemble, high-resolution global dataset of future climate projections. BC methods rely on the use of different statistical techniques to make climate model outputs more realistic at finer spatial

resolution by exploiting the available high resolution observation datasets (Ehret *et al.* 2012; Hawkins *et al.* 2013). BC can be typically implemented in several ways, including delta change, quantile mapping, linear regression, variance scaling, etc. The delta change method is the simplest approach and involves applying a changing factor to the historical observation for constructing a new time series of the future climate (Hawkins *et al.* 2013). A changing factor can be additive (difference) or multiplicative (ratio). Different changing factors can be employed for different climate variables. This method does not take into account changes in climate variability such as increasing extreme rainfall or longer dry spells. Linear regression performs

Table 2. List of regions used in this study (Giorgi and Francisco, 2000). Only land grid points are used in the analysis.

Name	Acronym	Latitude (°)	Longitude (°)
Australia	AUS	45S–11S	110E–155E
Amazon Basin	AMZ	20S–12N	82W–34W
Southern South America	SSA	56S–20S	76W–40W
Central America	CAM	10N–30N	116W–83W
Western North America	WNA	30N–60N	130W–103W
Central North America	CNA	30N–50N	103W–85W
Eastern North America	ENA	25N–50N	85W–60W
Alaska	ALA	60N–72N	170W–103W
Greenland	GRL	50N–85N	103W–10W
Mediterranean Basin	MED	30N–48N	10W–40E
Northern Europe	NEU	48N–75N	10W–40E
Western Africa	WAF	12S–18N	20W–22E
Eastern Africa	EAF	12S–18N	22E–52E
Southern Africa	SAF	35S–12S	10W–52E
Sahara	SAH	18N–30N	20W–65E
Southeast Asia	SEA	11S–20N	95E–155E
East Asia	EAS	20N–50N	100E–145E
South Asia	SAS	5N–30N	65E–100E
Central Asia	CAS	30N–50N	40E–75E
Tibet	TIB	30N–50N	75E–100E
North Asia	NAS	50N–70N	40E–180E

a regression analysis using historical observations and climate model outputs during the same period and applies the regression parameters to construct bias-adjusted future climate time series. The regression can be made as simple or complex (Belitz and Stackelberg, 2021). Quantile mapping generally uses a Gaussian or gamma distribution function to correct the distribution function of a climate variable and improve its fitting to observations (Teutschbein *et al.* 2012; Themeßl *et al.* 2011). Quantile mapping has become widely used because of its ability to correct bias at the extreme tails and its desired accuracy and robustness. However, the results may be sensitive to the choice of calibration period.

Here we use the delta change method as our BC method. The basic principle behind the BC delta method involves adding changes (or delta) in projected monthly climate to the high-resolution present-day climate (baseline). The projected monthly climate from the IGSM is at the coarse resolution (zonal) and need be spatially disaggregated to match the high-resolution baseline climate before the addition is applied. The spatial disaggregation is achieved through a pattern-scaling technique (section 3.2). The change is defined as the difference between the spatially-disaggregated monthly climate in the future and its long-term (20-year) monthly climatology in the historical period. The delta method assumes that changes in climates are only relevant at coarse scales but temporal variability of each variable is maintained towards the future. This assumption may hold true in many cases, except for the highly heterogeneous landscapes where considerable variations may be induced within a relatively short distance. The low computational demand of the delta method allows for efficient bias-correction of large ensembles and diverse emission scenarios over centuries.

The method comprises the following steps: (1) detrending the time series of monthly baseline climate (GSWP3, 1931-2010) for each month and each climate variable at each grid; 2) extracting the IGSM zonal historical (2001-2020) and projected (2021-2100) monthly climate; 3) spatially disaggregating 2) to the spatial resolution of the baseline climate (0.5°) based on a "pattern scaling" method tailored to the IGSM configuration (Schlosser *et al.* 2012) and determining the changes (deltas) in the projected monthly climate; and 4) Adding the spatially disaggregated changes in the projected monthly climate (3) of 2021-2100 to the corresponding detrended baseline climate (1) of 1931-2010. The procedure is implemented for each ensemble member and emission scenario. Details for each step are elaborated below.

3.1 Detrend Baseline Climate

We perform significance test for the linear trend of 80-year (1931-2010) GSWP3 monthly time series for each month and each climate variable at each grid. If a linear trend is found to be statistically significant at the 95% confidence level, the new monthly time series are derived by first detrending the original monthly time series and then adjusting (adding) the detrended monthly values to the corresponding monthly values of year 2020 to emulate an 80-year (2021-2100) climate without climate change. The monthly values of year 2020 are obtained based on the linear trend. If a linear trend is found to be not statistically significant, the new monthly time series will simply take the original monthly time series. The derived new monthly time series of all the months are then merged, which is referred to as "detrended baseline climate" in the following steps. For precipitation, we transform monthly precipitation in logarithmic scale. A linear relationship is examined only if at least half of the total years (80) have the pre-transformed monthly precipitation larger than 1 mm/day. This condition

will prevent any artificial linear trend as a result of very low precipitation amount in very dry areas (e.g., Sahara Desert), which could lead to unrealistically high values in the detrended precipitation time series. Detrending (if a linear trend is significant) is only applied to the years that involve in constructing the linear relationship. Other years will simply take the corresponding monthly values of year 2020.

3.2 Pattern-scaling

The MIT IGSM provides a 50-member ensemble of climate projections at the zonal level, which is expanded across longitudes using a pattern-scaling method as follows to provide regional details (Schlosser *et al.* 2012).

$$\bar{V}_{x,y} = \bar{C}_{x,y} * \bar{V}_y, \;\; V_{x,y} = \left(\bar{C}_{x,y} + \left[\frac{dC_{x,y}}{dT_G} * \Delta T_G \right] \right) * V_y \;\;\; (2)$$

Where $\bar{C}_{x,y}$ is the climatological downscaling transformation coefficient in a historical reference time period; $\bar{V}_y$ is the IGSM zonal monthly climatology of a variable at a given latitude (y) in a historical period; $\bar{V}_{x,y}$ is the transformed historical monthly climatology of the variable at a given longitude (x) along the latitude (y); V_y represents the IGSM zonal monthly future climate under a human-forced monthly global mean temperature change (ΔT_G); $V_{x,y}$ represents the corresponding transformed monthly future climate; $\frac{dC_{x,y}}{dT_G}$, namely "pattern-change kernels" (PCKs), describes the shifts in $\bar{C}_{x,y}$ induced by human-forced climate warming. In our study, $\bar{C}_{x,y}$ is derived from the 20-year (1991-2010) GSWP3 forcing and calculated as the ratios of monthly climatology at each grid to monthly climatology at the respective latitude band. $\bar{V}_y$ is calculated as the monthly climatology from 2001 to 2020. ΔT_G is calculated as the difference between 10-year backward moving average of global mean temperature and its respective 2012-2021 mean for each month. V_y (from January 2021 to December 2100) is calculated as the 20-year backward moving average for each month. For example, January 2021 is calculated as the average of January from 2002 to 2021. PCKs are constructed from the list of the CMIP6 climate models (Table 1), with each climate model regridded to a 0.5° common grid via area averaging (conservative regridding procedure) prior to PCKs construction. Each of the 18 constructed PCKs ($\frac{dC_{x,y}}{dT_G}$) is then combined with the 50-member IGSM climate projections (V_y) via the equation (2) to develop a 900-member ensemble per policy scenario. This meta-ensemble per scenario represents a comprehensive range of plausible outcomes resulting from the uncertainties in global climate responses (50-member ensemble of the IGSM zonal climate projections) and regional response pattern changes (PCKs). The change in the projected monthly climate ("delta") is the difference between $V_{x,y}$ and $\bar{V}_{x,y}$. The monthly change is further smoothed using a 21-year running average centered on each year for that month (the first and last 10 years have fewer samples for smoothing).

4. Results

4.1 Seasonal PCKs

Seasonal PCKs of temperature and precipitation show a wide range of climate model response patterns as a result of forced climate warming (**Figs 3-6**). The differences are reflected in the sign, magnitude, location, and extent of the change in response. For temperature (Figs 3-4), the most striking feature is a colder ocean and warmer land (COWL) global pattern (Broccolli *et al.* 1998) seen in both seasons across all the models, with the exceptions to this characterization found in different regions across various models. The model mean PCKs show that the relative cooling signal in land areas lies mostly over the northwestern-most regions of North America, western Europe, northern Siberia and parts of the southern Russia in DJF (Figure 4). The maritime fetch of the relatively cooler ocean conditions may play a large role in the afore-mentioned relative cooling over the coastal regions. Also evident is the stronger warming over the high Northern Hemisphere latitudes in DJF than in JJA. High inter-model scatter in PCKs is ubiquitously observed in the boreal region of the Northern Hemisphere, particularly in DJF. In JJA, South Africa and interior portions of South America also present moderate inter-model scatter. The lowest model scatter generally occurs over much of the world's oceans, particularly in the subtropics and with no evident seasonality. For precipitation (**Figs 5-6**), the model mean shows a wide extent of drier conditions attributed to climate warming, including a swath extending from central subtropical North Pacific to the North Atlantic and a path extending from the South Pacific basin to the South Atlantic and the Indian Ocean. The drying feature in these regions persists in both seasons, with the areas of prominent drying varying between two seasons. The drying is particularly enhanced over central subtropical North Pacific and the North Atlantic in DJF, but it is more prominent over the central America, Gulf of Mexico, Caribbean Sea and islands, east Indian Ocean and Indonesia islands in JJA. Over land areas, the most prominent drying occurs over Mexico, northern South America, northern African, and parts of the Middle East in DJF, but is largely confined to the Continental United States, Amazon, Southern Africa, Australia, the European continent, and Western Russia in JJA. The wetter conditions in both seasons over land areas are largely associated with the monsoon regions, including South and Southeast Asia, Africa, Australia, South and North America. High model scatter for precipitation is largely confined to the world's oceans, particularly in DJF, including the subtropical Pacific, the western boundary of the North Atlantic, the tropical Atlantic, and the Indian Ocean. Over land, the Indian and Southeast Asian monsoon regions present the largest model scatter. Other notable areas with moderate model scatter include the eastern half of North America, most of Central America, South America, parts of Africa, Australia, Europe, and Western Russia. A large portion of Eurasia, Central North America, and Northern Africa contains the lowest inter-model deviations, particularly in DJF.
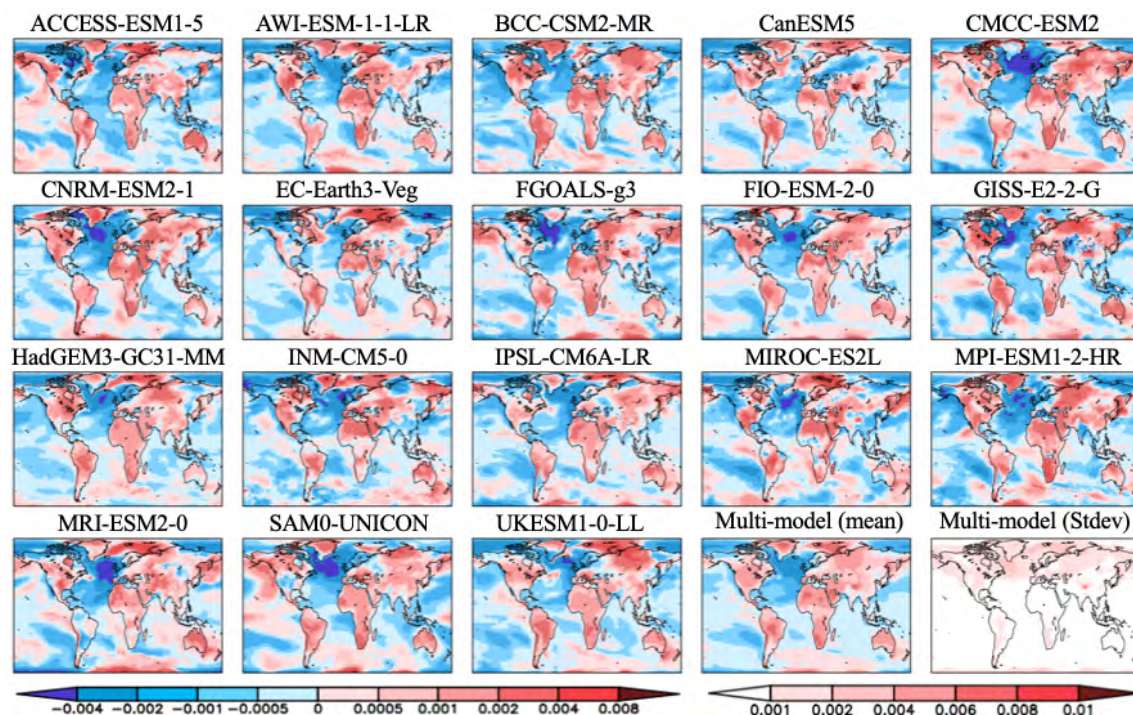

Figure 3. Global maps of the JJA averaged pattern-change kernels (PCKs) that describe the relative change in surface air temperature per unit change in global averaged surface-air temperature (units of K-1) from each of the 18 participating models in the Coupled Model Intercomparison Project Phase 6 (CMIP6) as well as the multi-model mean and standard deviation. PCKs are derived for each month from the 1% transient CO_2 experimental simulations.
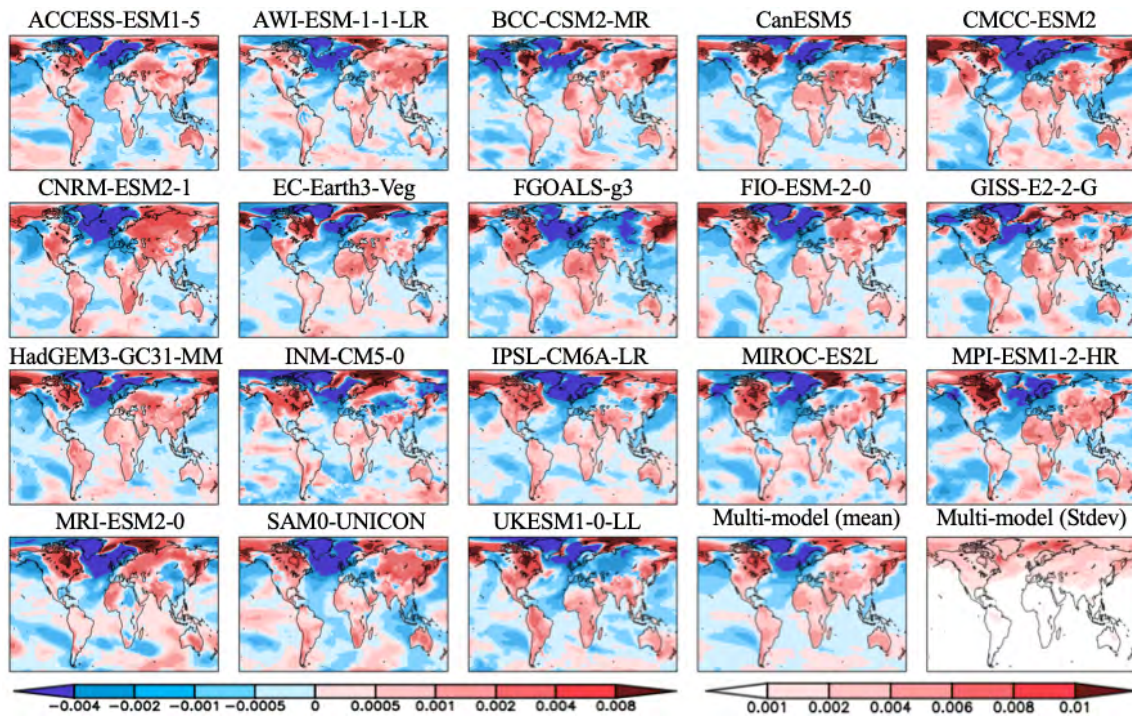
Figure 4. Same as Figure 3, but for the DJF averaged pattern-change kernels (PCKs).
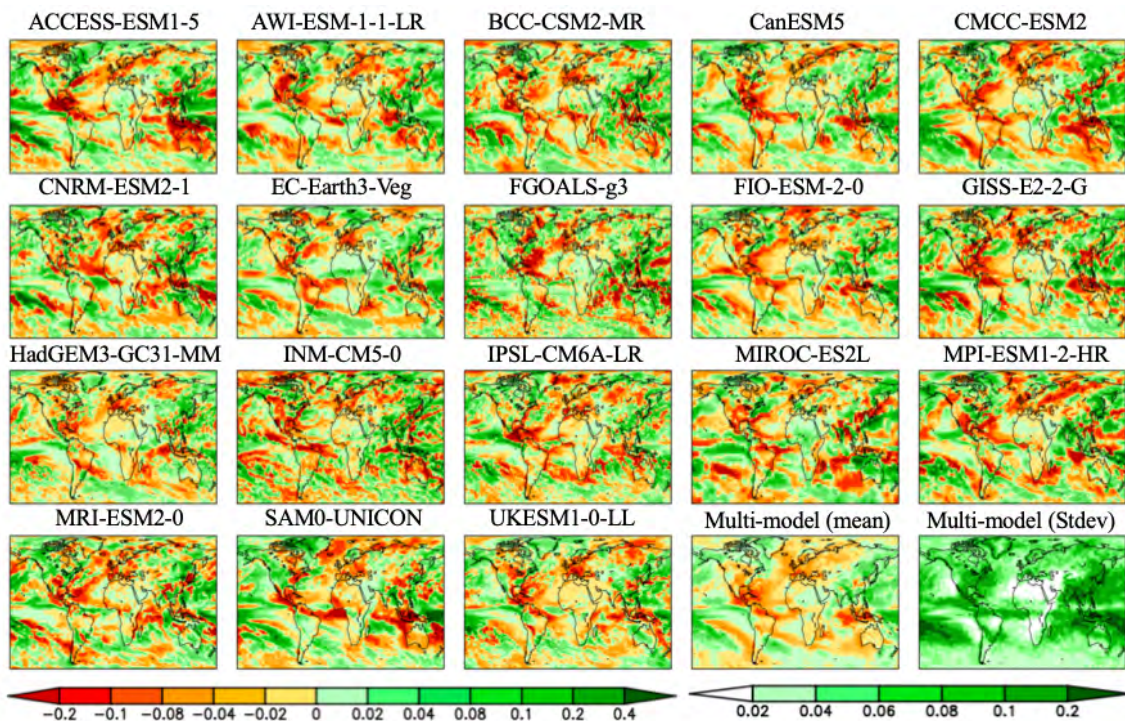

Figure 5. Global maps of the JJA averaged pattern-change kernels (PCKs) that describe the relative change in precipitation per unit change in global averaged surface-air temperature (units of K-1) from each of the 18 participating models in the Coupled Model Intercomparison Project Phase 6 (CMIP6) as well as the multi-model mean and standard deviation. PCKs are derived for each month from the 1% transient CO_2 experimental simulations.
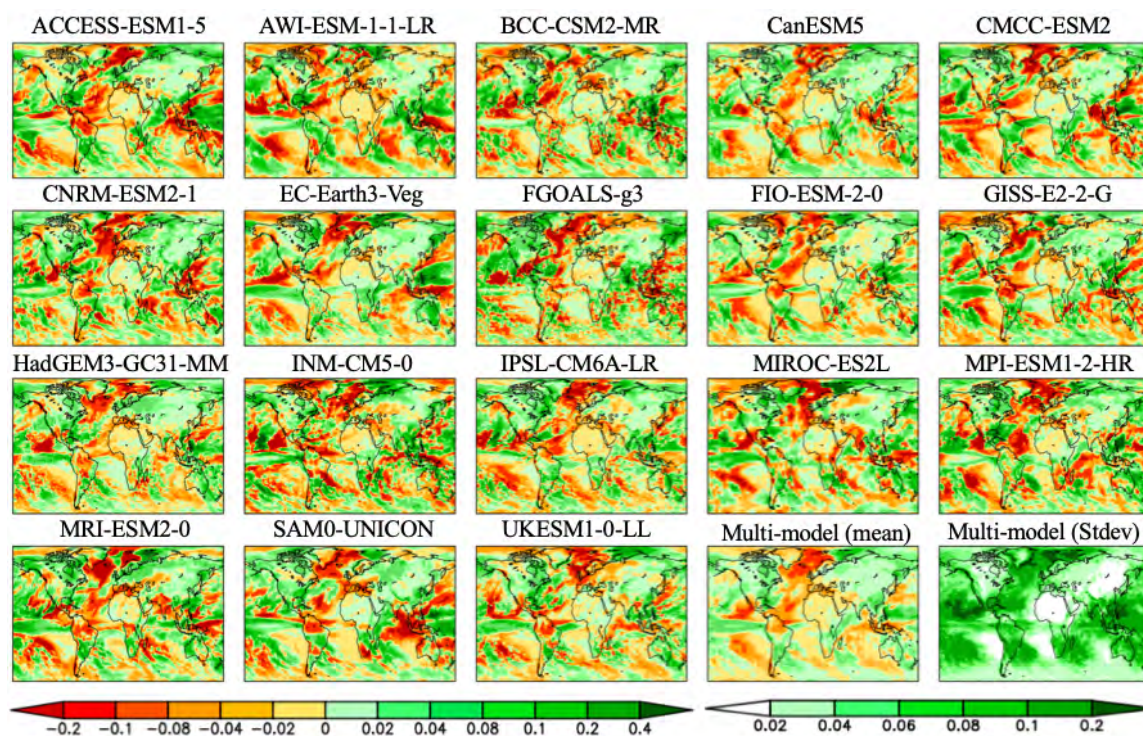
Figure 6. Same as Figure 5, but for the DJF averaged pattern-change kernels (PCKs).

4.2 Dataset Evaluation

Quantitative assessments are performed for all the meteorological variables and all the seasons [December-February (DJF), March-May (MAM), June-August (JJA), and September-November (NOV)] over the 21 regions in Table 2 from 1931 to 2010 (the detrended baseline) and from 2021 to 2100 (projected future climate) for four emission scenarios, respectively. Only precipitation and surface air temperature in DJF and JJA are included for demonstration purposes. Only land grid points are used in the assessments, except for the global maps shown in Figure 10.

4.2.1 Baseline Climate

Figure 7 shows the comparisons of precipitation and surface air temperature between GSWP3 and detrended baseline from 1931 to 2010 over the 21 regions. Overall, both JJA and DJF GSWP3 precipitation does not show evident trends over all the regions, except for the JJA precipitation in WAF and EAF (Figure 7a, b). We see that the corresponding detrended baseline precipitation eliminates or reduces the trends in these two regions. Detrending is more clearly observed in the surface air temperature (Figure 7c, d). As expected,

GSWP3 surface air temperature exhibits strong upward trends over a majority of regions for both seasons. Some exceptions are observed for SSA, North America (WNA, CAN, ENA), GRL, and NEU in both seasons, for Asia (except for CAS) and TIB in JJA, as well as for WAF, SAH, and NAS in DJF. GSWP3 surface air temperature in DJF presents overall weaker upward trends than in JJA, except for EAS, SAS, and TIB. Regions in the same continent may display very different patterns. For example, CAS is only one out of four regions in Asia showing a strong upward trend in the JJA temperature. Other variables (shortwave and longwave radiation, wind speed) in both seasons may exhibit upward or downward trends in the scattered regions (not shown). An additional notable feature is that the GSWP3 specific humidity in both seasons are largely associated with weak upward trends with small changes in the magnitude across the entire period (not shown). Such upward trends are consistent with those in surface air temperature as warmer temperature makes the atmosphere hold more water vapor. Overall, the detrended baseline climate is seen to eliminate or reduce the trends inherent in the GSWP dataset to varying degrees, regardless of the meteorological variables, seasons, and regions.
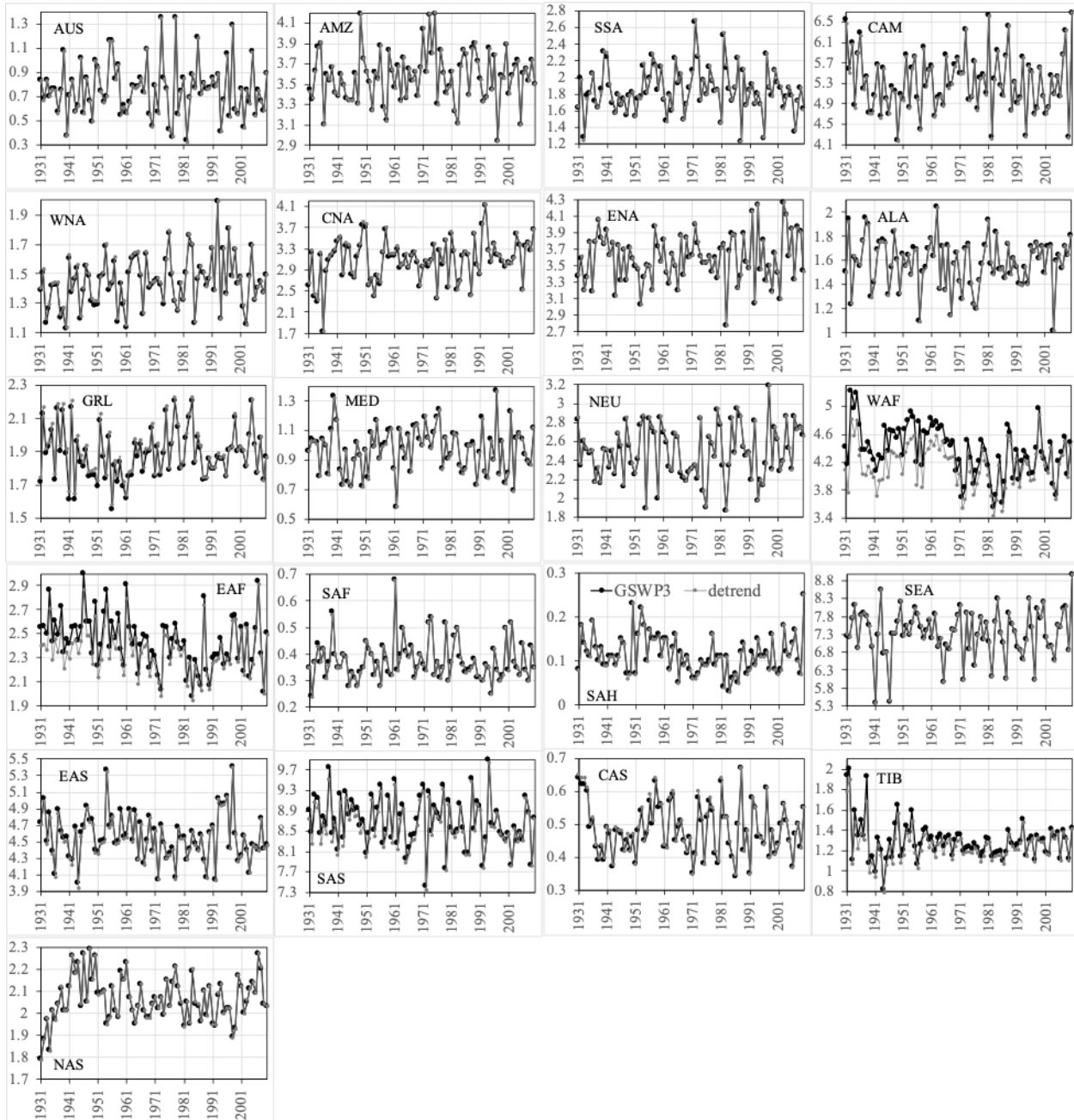
Figure 7a. Comparisons between the JJA GSWP3 (black line) and detrended baseline (gray line) precipitation (mm/day) from 1931 to 2010 over the 21 regions.
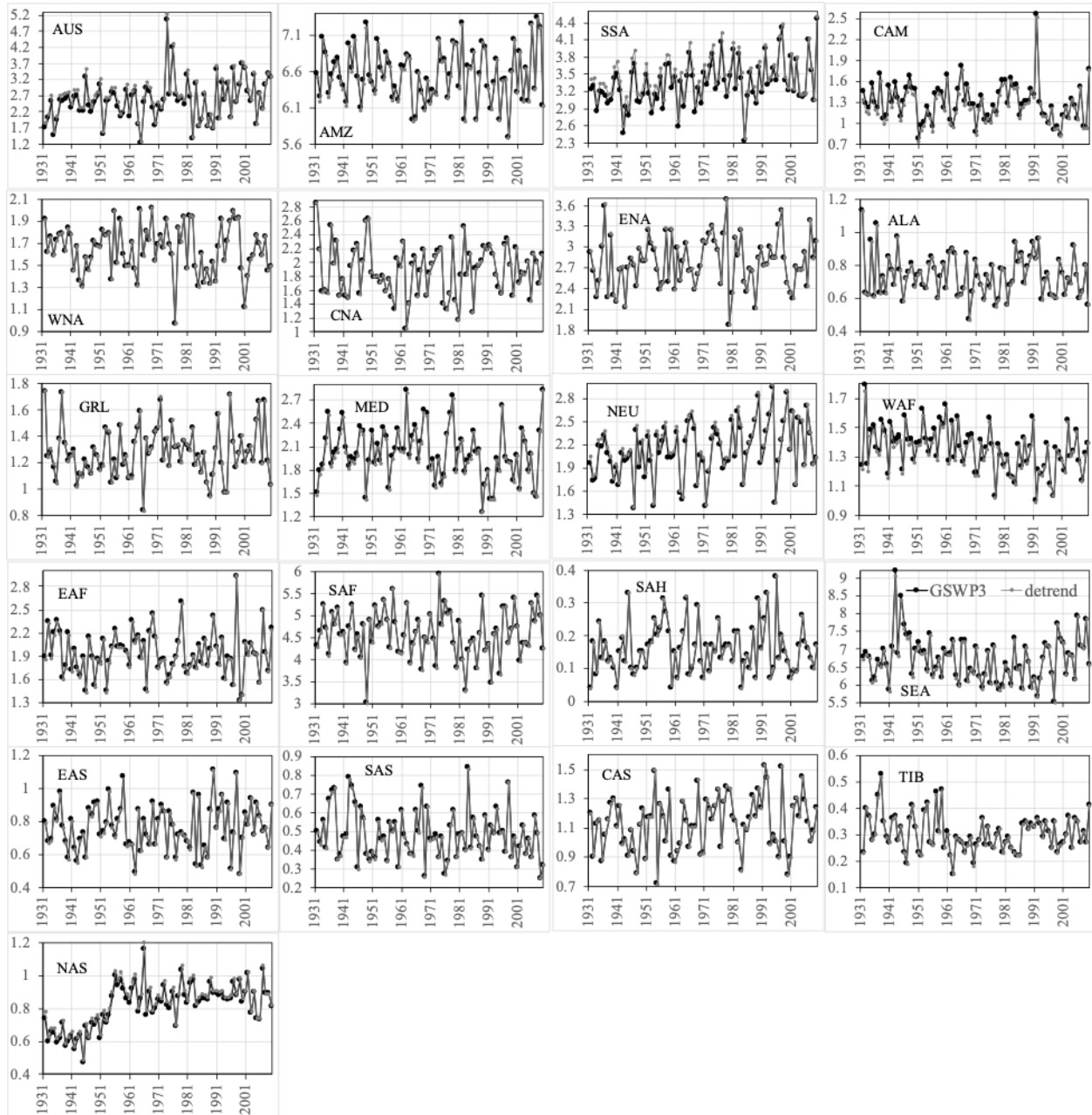
Figure 7b. Comparisons between the DJF GSWP3 (black line) and detrended baseline (gray line) precipitation (mm/day) from 1931 to 2010 over the 21 regions.
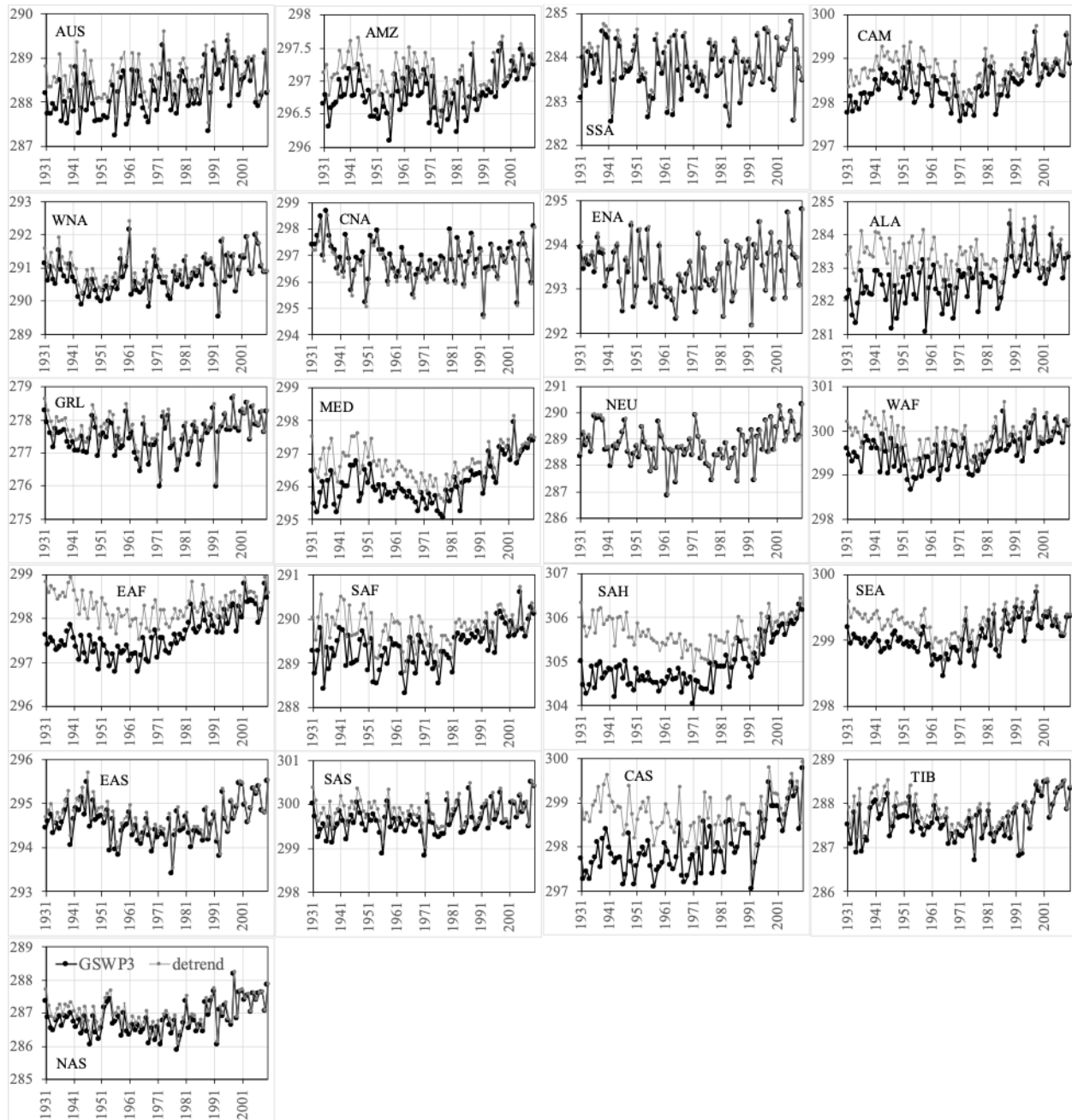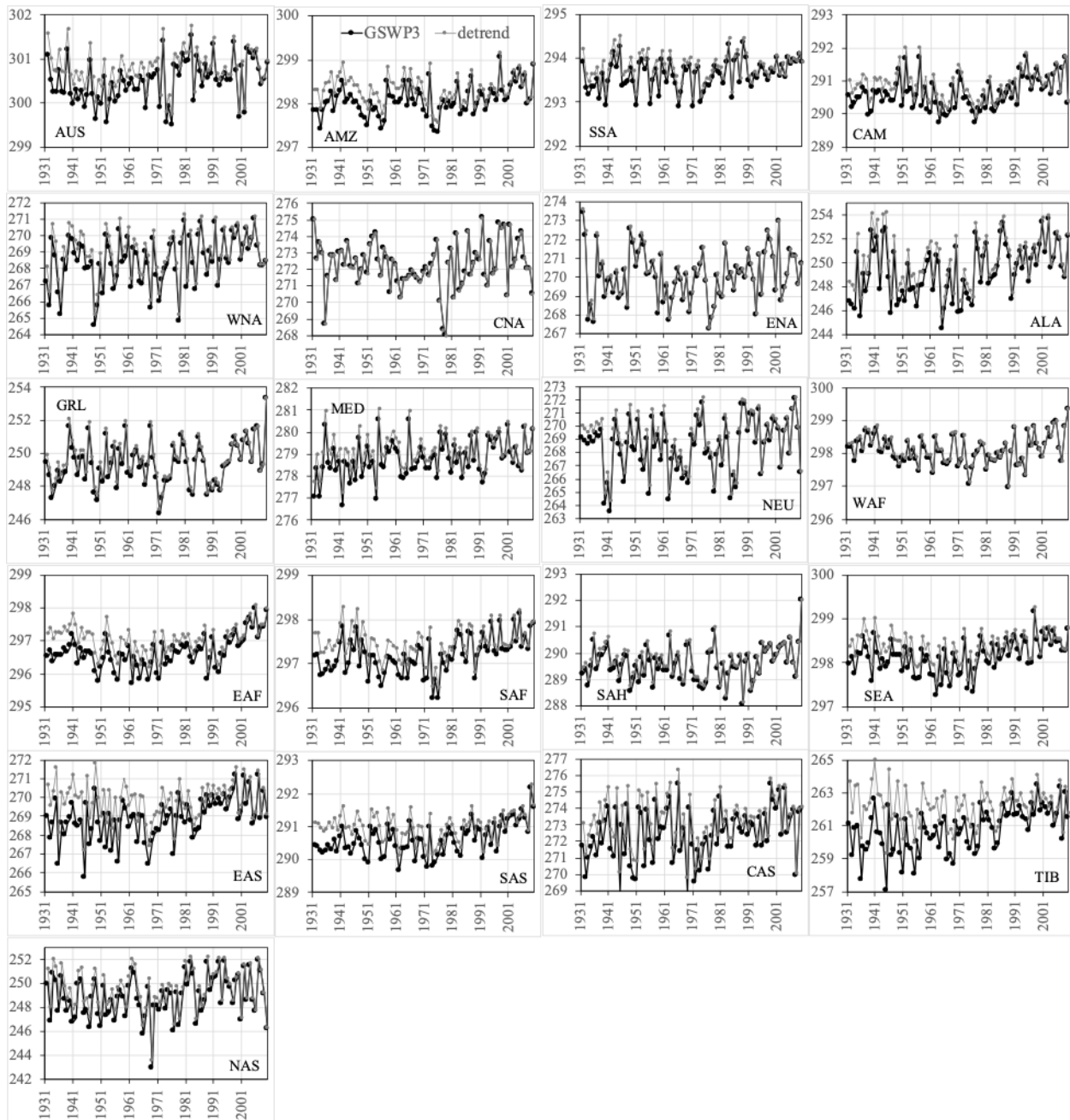
Figure 7c. Comparisons between the JJA GSWP3 (black line) and detrended baseline (gray line) near-surface air temperature (K) from 1931 to 2010 over the 21 regions.

Figure 7d. Comparisons between the DJF GSWP3 (black line) and detrended baseline (gray line) near-surface air temperature (K) from 1931 to 2010 over the 21 regions.

4.2.2 Future Climate

Figure 8 shows the ensemble statistics (minimum, median, and maximum) of precipitation and surface air temperature in both seasons from 2021 to 2100 for the PF scenario, along with their detrended baseline counterparts. The responses of projected precipitation to the human-induced warming are mixed across various regions. We see ensemble medians are largely aligned with the detrended baseline over a majority of regions (Figure 8 a, b). Some exceptions are found in the high latitudes (ALA, GRL, NEU, and NAS) and dry regions (EAF, SAH, and SAS in JJA as well as WNA, CNA, and ENA,

EAS, SAS, and TIB in DJF), where the detrended baseline values are just aligned with the ensemble minimums or fall outside the projected precipitation ranges marginally. This is likely an indication that current climate models present some difficulties in representing the precipitation in these regions. As expected, the ensemble uncertainty (spread) over all the regions is small at the beginning of the period and becomes increasingly larger by the end of the century. The high latitude and dry regions are typically characterized by the small ensemble uncertainty in both seasons. The large ensemble uncertainty is generally found around the tropics, such as CAM (3.66 mm/day) and SEA (2.87 mm/day) in
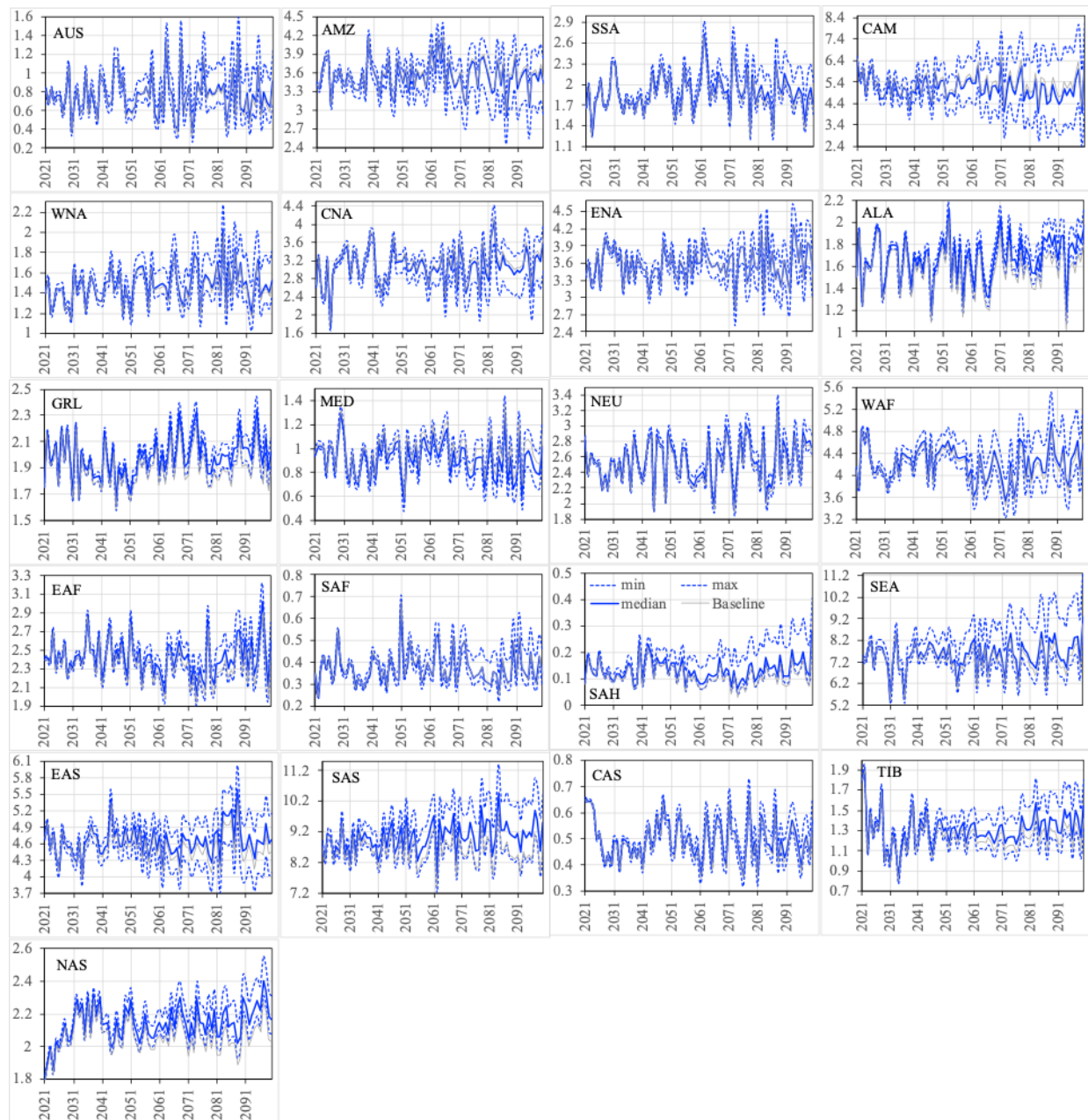

Figure 8a. The ensemble statistics (minimum, median, and maximum) of the JJA precipitation (mm/day) from 2021 to 2100 over the 21 regions for the PF scenario, along with their detrended baseline counterparts.

JJA as well as SEA (1.54 mm/day) and AMZ (1.18 mm/day) in DJF, consistent with what was found in previous studies (Kharin *et al.*, 2013; O'Gorman, 2012; Sillmann *et al.*, 2013).

It is not surprising that all the ensemble members exhibit consistently higher surface air temperature than the detrended baseline throughout the entire period in both seasons over all the regions (Figure 8 c, d). The tropical regions present an overall smaller ensemble uncertainty in both seasons. The ensemble spread of the JJA air temperature varies from 1.13°C in the SEA to 3.16°C in the CNA by 2100. TIB is the only other region with the ensemble uncertainty of the JJA air temperature exceeding 3°C (3.02°C). The

uncertainty of the JJA air temperature in the CNA may be associated with the differences in modeled trends and responses to precipitation-recycling ratios, dependencies on the boundary layer parameterization, and the land model representation of evapotranspiration, while that in the TIB is likely attributed to the model differences in representing orographic effects. The DJF air temperature features the large ensemble uncertainty in the high latitudes, particularly in the GRL (4.7°C) and ALA (4.9°C) regions, and underscores the influence from the heterogeneity in the representations of snow and cold land processes by various Earth-system models (Slater *et al.*, 2001; Luo *et al.*, 2004).
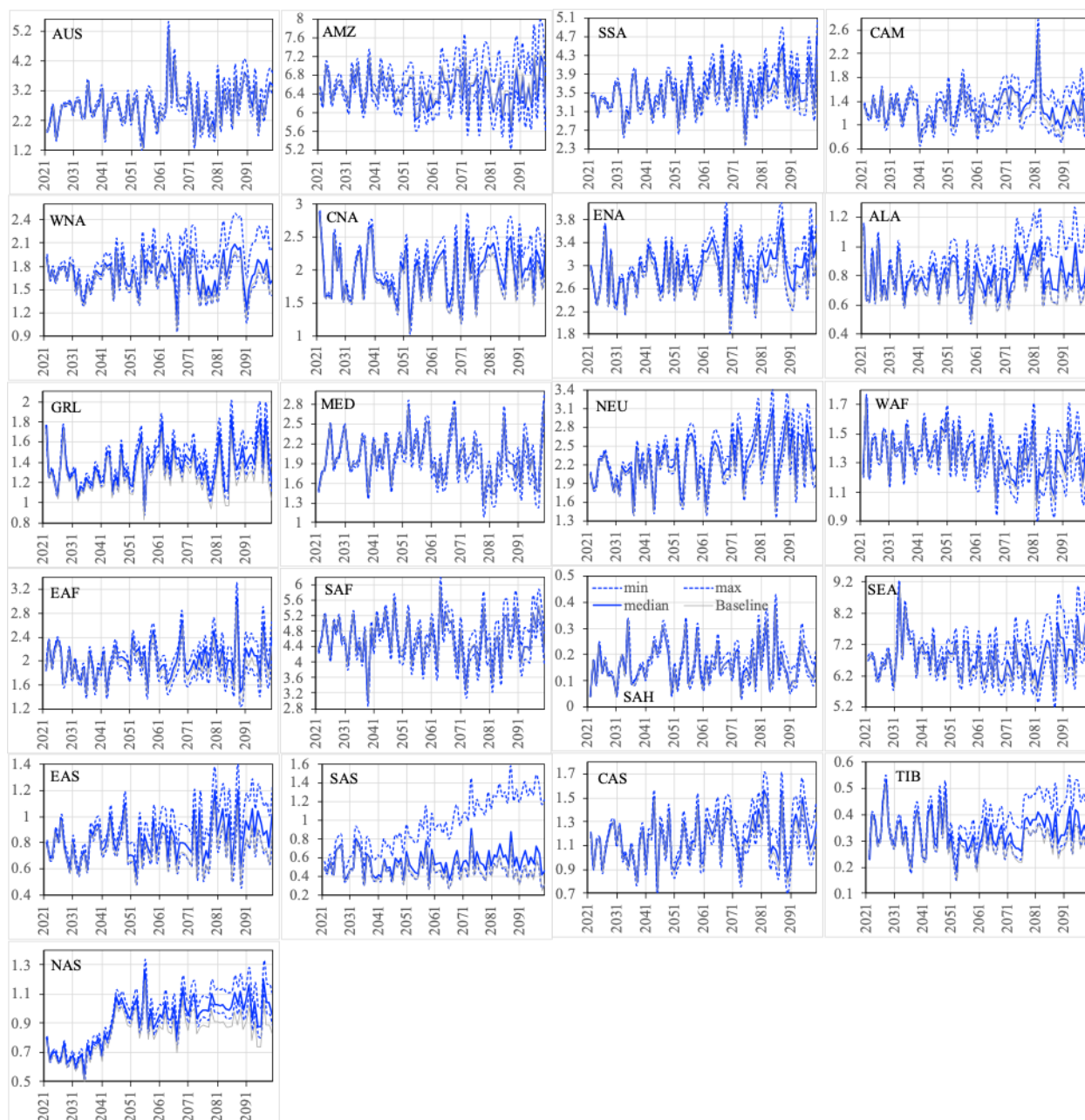

Figure 8b. The ensemble statistics (minimum, median, and maximum) of the DJF precipitation (mm/day) from 2021 to 2100 over the 21 regions for the PF scenario, along with their detrended baseline counterparts.
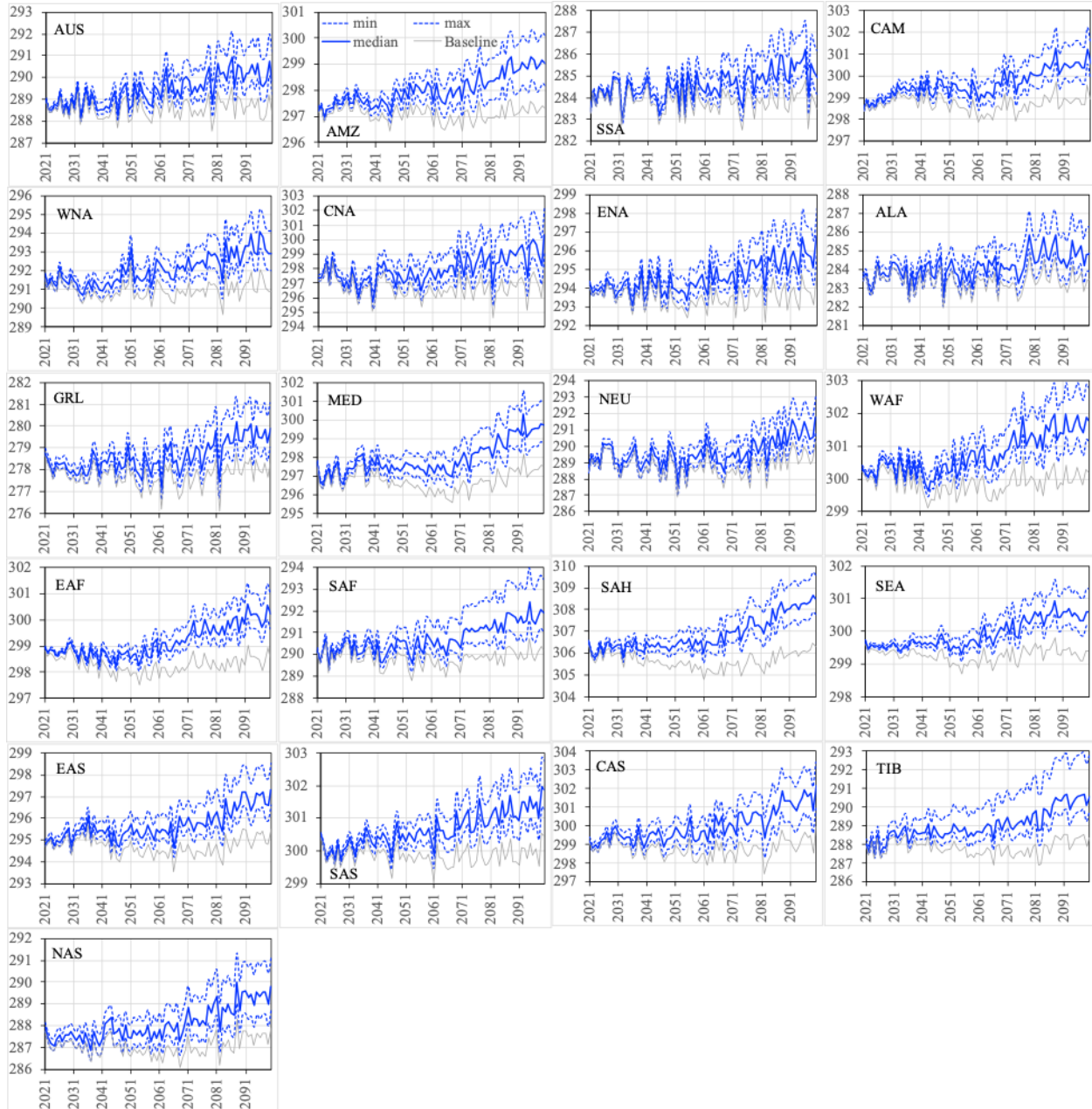
Figure 8c. The ensemble statistics (minimum, median, and maximum) of the JJA surface air temperature (K) from 2021 to 2100 over the 21 regions for the PF scenario, along with their detrended baseline counterparts.
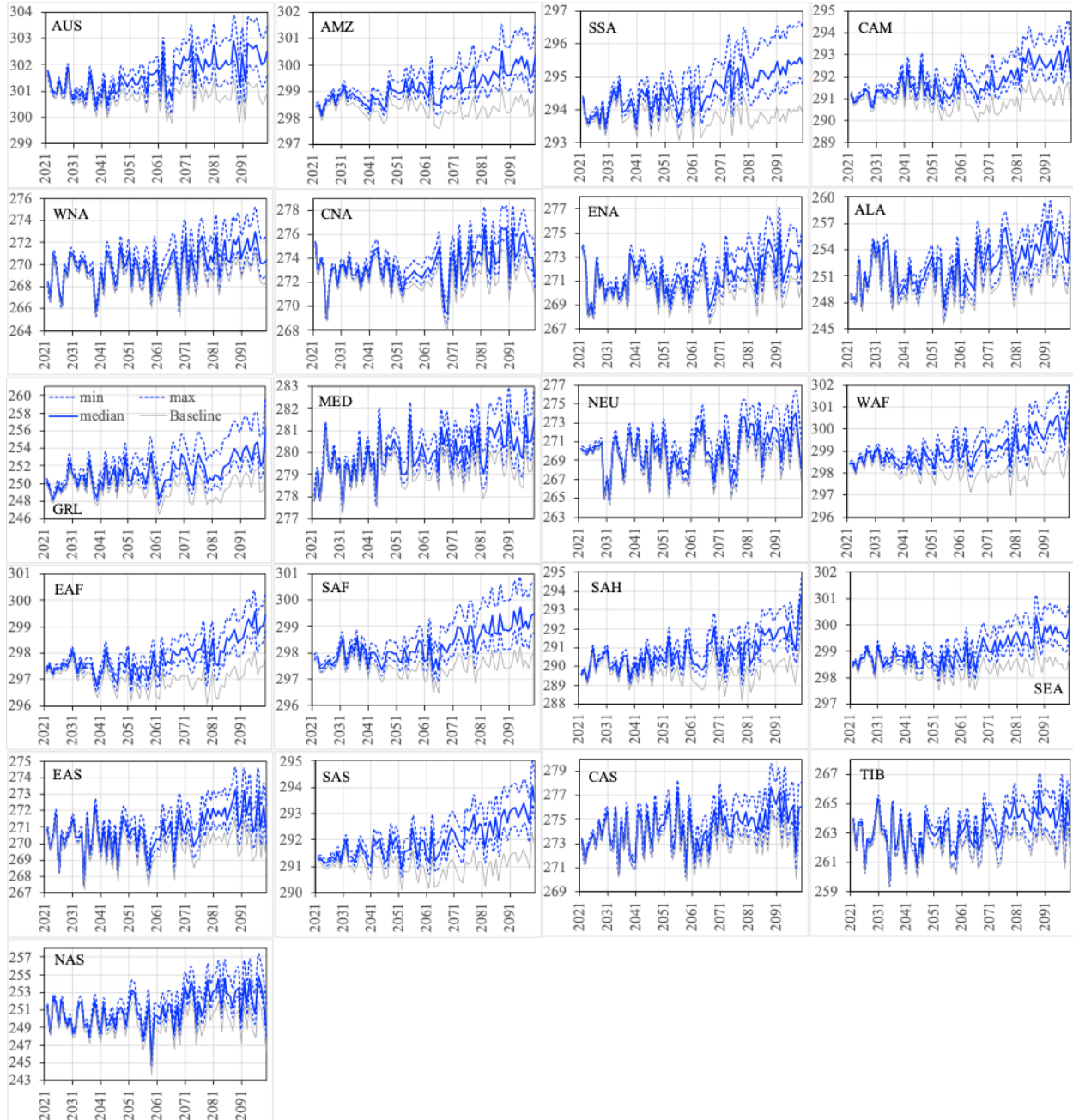
Figure 8d. The ensemble statistics (minimum, median, and maximum) of the DJF surface air temperature (K) from 2021 to 2100 over the 21 regions for the PF scenario, along with their detrended baseline counterparts.

Figure 9 shows the ensemble medians of precipitation and surface air temperature in both seasons from 2021 to 2100 for all the four scenarios, along with their detrended baseline counterparts. We see that the differences in precipitation of both seasons (Figure 9 a, b) attributed to the scenarios are much smaller than those attributed to the ensembles of the specific scenario (e.g., PF in Figure 8). By 2100, the spread of the JJA precipitation across four scenarios (the difference between REF and P1p5C) is less than 0.2 mm/day over most of the regions, except

for CAM (-0.47), SEA (0.24), and SAS (0.49) (Figure 9a). For the most aggressive policy scenario (P1p5C), 5 out of 21 regions experience slight wetting trends in JJA relative to no policy scenario (REF), including ENA (-0.04), AMZ (-0.06), MED (-0.1), CNA (-0.14), and CAM (-0.47). The spread in the DJF precipitation is even smaller, ranging from -0.1 to 0.26 mm/day across various regions (Figure 9b). Overall, precipitation of both seasons does not exhibit apparent drying or wetting trend over all the regions with climate policy in place as compared to no policy. In contrast,
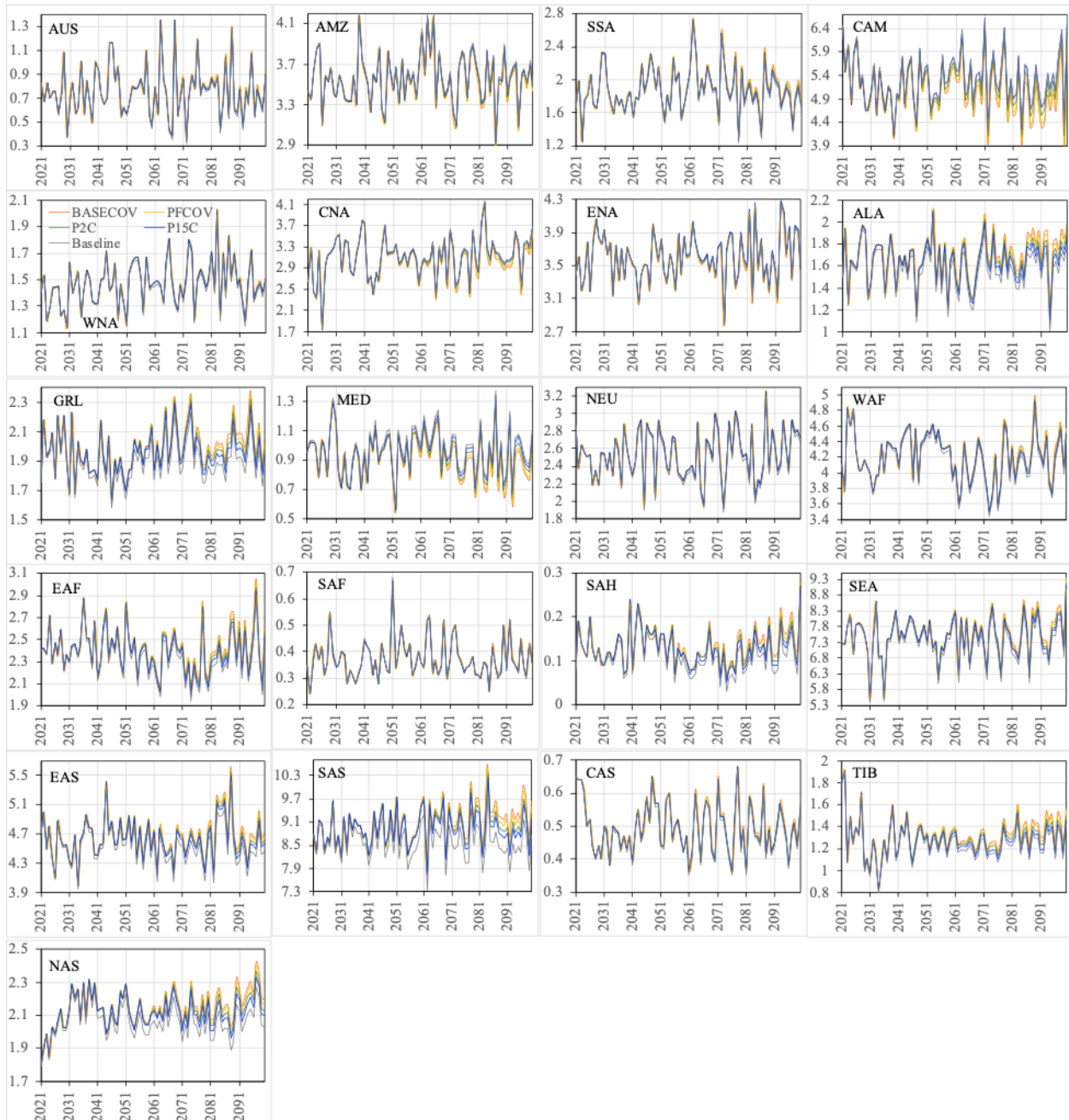

Figure 9a. The ensemble medians of the JJA precipitation (mm/day) from 2021 to 2100 over the 21 regions for all the four policy scenarios, along with their detrended baseline counterparts.

climate policy (P1p5C) shows strong mitigation effect on surface air temperature, with the reduction ranging from 1.1°C to 1.9°C in JJA (Figure 9c) and from 1.0°C to 2.9°C in DJF (Figure 9d) across various regions. The strongest reduction in the JJA air temperature occurs mostly in the mid latitudes (e.g., CNA, CAS, MED, TIB) and SAH desert, while that in the DJF air temperature is found mostly in high latitudes (2.9°C in ALA, 2.5°C in GRL, 2.4°C in NAS, 1.9°C in ENA). Many studies documented "Arctic

amplification", a phenomenon that the warming in the Arctic far outpaces the global average (Post *et al.*, 2019; Rantanen *et al.*, 2022), particularly in winter (Bintanja and Krikken, 2016). Our results suggest that climate mitigation policy can effectively slow or reduce warming in these regions and would have significant implications on land and sea ice, wildlife and human livelihoods, methane emissions, and extreme weather at lower latitudes.
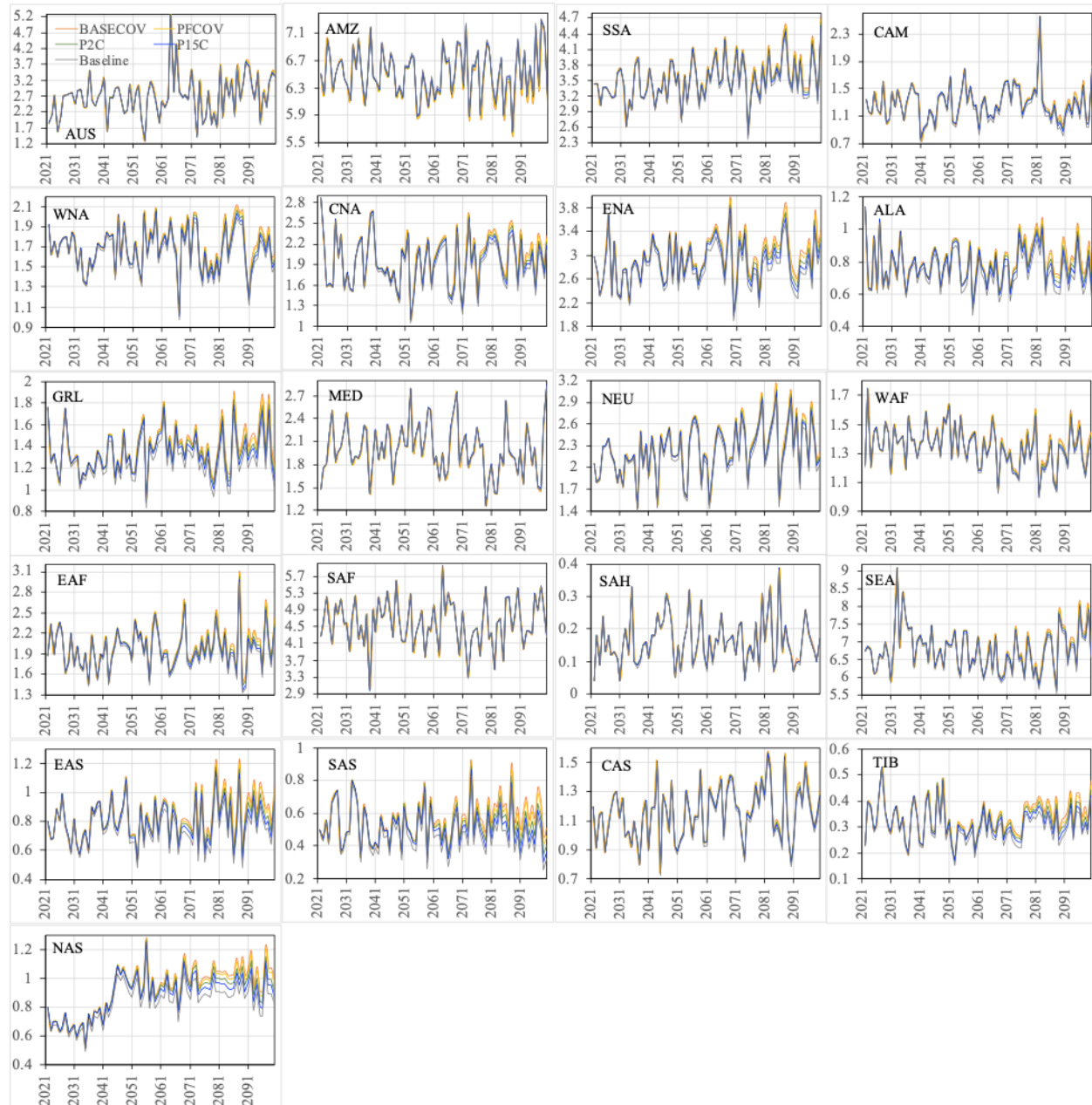

Figure 9b. The ensemble medians of the DJF precipitation (mm/day) from 2021 to 2100 over the 21 regions for all the four policy scenarios, along with their detrended baseline counterparts.
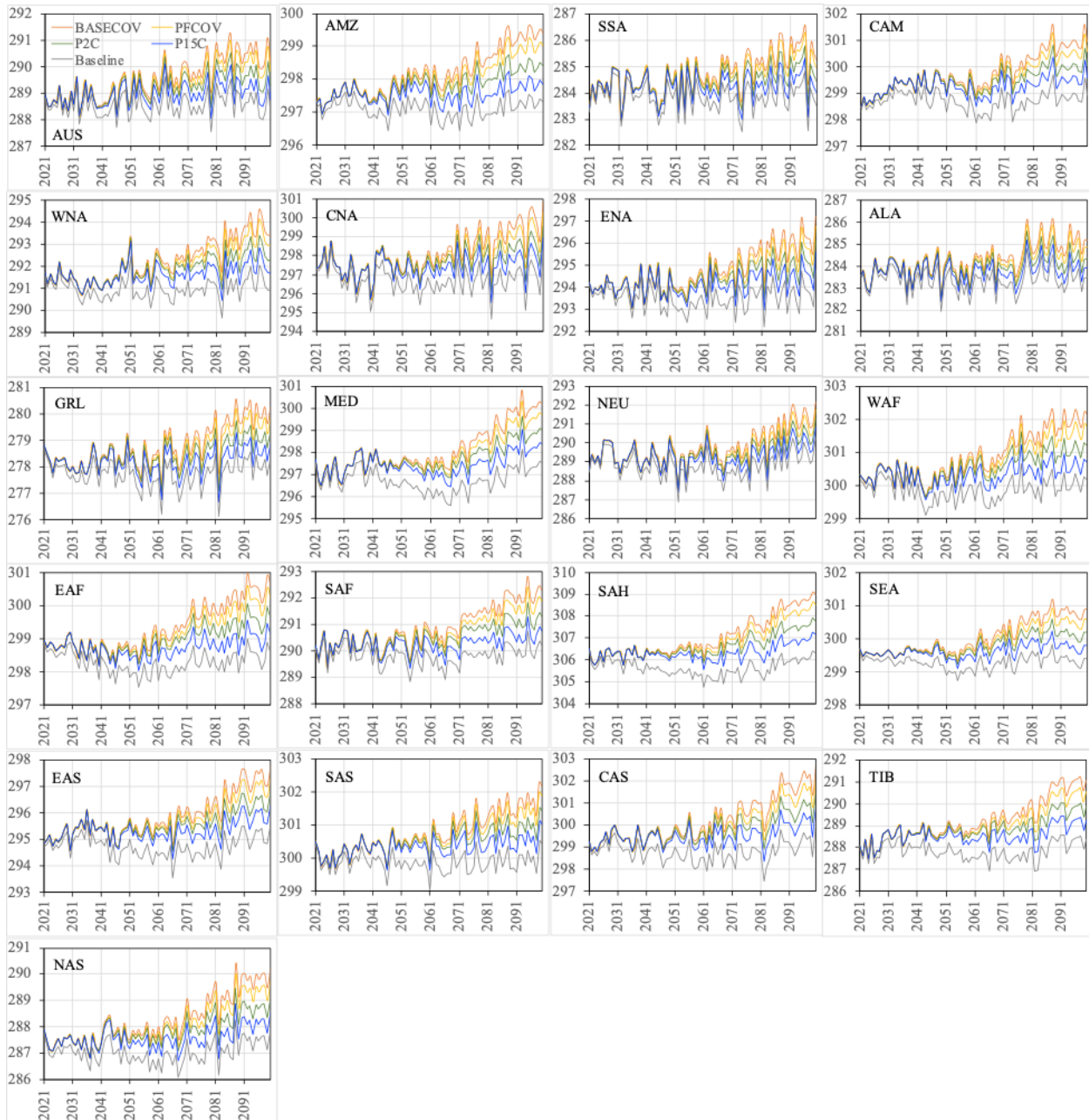
Figure 9c. The ensemble medians of the JJA surface air temperature (K) from 2021 to 2100 over the 21 regions for all the four policy scenarios, along with their detrended baseline counterparts.
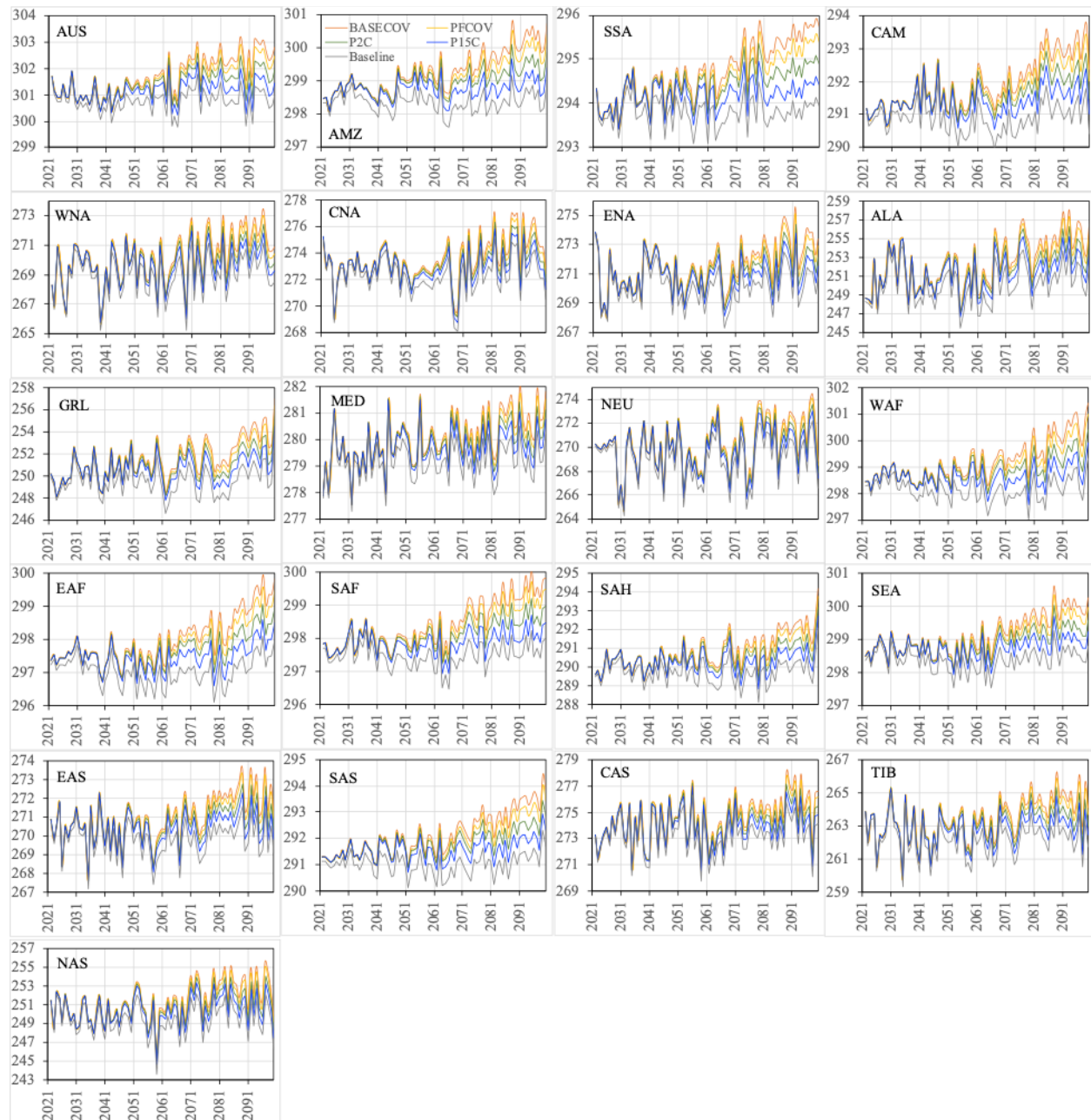
Figure 9d. The ensemble medians of the DJF surface air temperature (K) from 2021 to 2100 over the 21 regions for all the four policy scenarios, along with their detrended baseline counterparts.

Table 3 summarizes 5-year mean differences (centered in 2050 and 2090) in the ensemble medians of REF from those of P1p5C and detrended baseline for 6 meteorological variables in JJA over 21 regions. Regardless of the periods, no climate policy (REF) always results in higher air temperature, longwave radiation, and specific humidity than P1p5C and detrended baseline. The increases in the JJA air temperature relative to the detrended baseline range from 0.5°C to 1.0°C in 2050 and 1.4°C to 2.7°C in 2090 across the regions, respectively. The most aggressive climate policy mitigates such increases by 0.1°C ~ 0.3°C (difference between REF and P1p5C) in 2050 and 1.0°C to 1.8°C in 2090, respectively. For the JJA longwave radiation, the increases in REF relative to the detrended baseline range from 3 to 7 W/m^2 in 2050 and 8 to 20 W/m^2 in 2090 across the regions, respectively. The increases are lowered by 1 to 2 W/m^2 in 2050 and 6 to 14 W/m^2 in 2090, respectively, attributed to the most aggressive climate policy. For specific humidity, the increases without climate policy relative to either scenario are relatively small over all the regions during both periods (0 ~ 0.0015 kg/kg). Other variables (precipitation, shortwave radiation, and wind speed) show mixed responses. Over a major of regions, the JJA precipitation and shortwave radiation without climate policy exhibits marginal increasing trends relative to P1p5C and detrended baseline. The two largest increases in 2090 occur in SAS (0.5 and 0.9 mm/day relative to P1p5C and detrended baseline, respectively) and SEA (0.2 and 0.4 mm/day) for precipitation, and in MED (4 and 11 W/m^2) and ENA (5 and 10 W/m^2) for shortwave radiation. These patterns are also observed in 2050 over the same regions but with smaller magnitudes. More than half of the regions demonstrate the decreasing JJA wind speeds in both periods without climate policy relative to P1p5C and detrended baseline. However, the maximum changes in the magnitudes are marginal across all the regions (< ± 0.05 m/s). The DJF climate variables present similar characteristics to its JJA counterparts (**Table 4**), except that 1) the air temperature increases without climate policy are higher in the upper bounds (0.5°C versus 0.3°C relative to P1p5C in 2050, 1.8°C versus 1.0°C relative to the detrended baseline in 2050, 2.7°C versus 1.8°C relative to P1p5C in 2090, and 4.1°C versus 2.7 °C relative to the detrended baseline in 2090), which is largely attributed to the high latitude regions; 2) the two largest increases in 2090 occur for precipitation in ENA (0.2 and 0.3 mm/day relative to P1p5C and the detrended baseline, respectively) and SEA (0.2 and 0.2 mm/day), and for solar radiation in AMZ (3 and 4 W/m2) and CAM (2 and 4 W/m2). These results (precipitation and air temperature) are consistent with what are present in Figure 9.

Figure 10 presents the ensemble medians of precipitation and surface air temperature in both seasons in 2090 for the PF scenario, along with the differences from its correspond-

ing detrended baseline counterparts. The ensemble median precipitation in both seasons indicate that maxima occur in the Tropics, specifically the intertropical convergence zone (ITCZ) in the Atlantic, Pacific, and Indian Oceans, the South Pacific convergence zone (SPCZ), as well as over tropical Africa and South America (**Figure 10 a, b**). This band of heavy rain moves north and south of the Equator seasonally. Major precipitation peaks in tropical regions are below the equator in DJF but are located further north in JJA. JJA is the season that is strongly affected by the Asian monsoon which brings heavy rain to China, southeast Asia, and India. In midlatitudes, the storm tracks in the Northern Hemisphere (NH) oceans are much stronger in DJF than in JJA, while the circumpolar storm tracks in the Southern Hemisphere (SH) are weaker in DJF than in JJA. DJF is also characterized by a secondary precipitation maximum along the northwest coast of North America from Alaska to California at the eastern end of the Pacific Ocean storm track. Except for the Maritime Continent, a majority of land areas are characterized by dry condition in both seasons with moderate precipitation found in Eastern North America, northern Europe, northeastern and southeastern China in JJA.

The changes in the ensemble median precipitation relative to the detrended baseline are embedded with distinct zonal patterns inherited from the MESM zonal architecture (**Figure 10 c, d**). Nevertheless, many expected regional characteristics of wetting and drying are observed and shared by both seasons. The strongest positive changes are found in the equatorial Pacific with many regions being associated with Monsoon precipitation and they shift slightly between north and south seasonally. Extensive but weaker positive changes are also observed in the high latitudes (lands and oceans) of both hemispheres, likely attributed to the increased specific humidity of the warmer troposphere and increased transport of water vapor from the tropics. A strong drying signal is projected over the central America, the Amazon, the Mediterranean, and Indonesia islands together with the Atlantic, Indian, and South Pacific Oceans. The most part of the United States (US) is projected to become wetter in DJF, particularly in the Eastern US and the west coast, while many regions will experience precipitation decreases in JJA, including the northern part of the country (40° ~ 50°N) and the southern US. In-between lies a moderate wetting zone extending from the Southwestern to the Southeastern US.

The ensemble medians of the JJA and DJF surface air temperature (**Figure 10 e, f**) demonstrate the well-established temperature gradient from the equator to the high latitudes of both hemispheres. The JJA temperature maxima are located in the Sahara Desert, the Middle East, the Mojave Desert, and the Sonoran Desert in northwestern Mexico, while the temperature minima are confined to the Greenland and

Table 3. 5-year mean differences between the ensemble medians of REF and P1p5C (top row of each region) as well as REF and detrended baseline (bottom row of each region) for 6 meteorological variables in JJA over 21 regions. 5-year mean is centered in 2050 (2048~2052) and 2090 (2088 ~ 2092), respectively. Negative values indicate lower values in REF relative to P1p5C (top row) or detrended baseline (bottom row). The difference between bottom row and top row represents mitigation effects with the most aggressive climate policy relative to no policy scenario.

Region	Prep (mm/d)		Tbot (°C)		Fsds (W/m2)		Flds (W/m2)		Wind (m/s)		Qbot (kg/kg)	
	2050	2090	2050	2090	2050	2090	2050	2090	2050	2090	2050	2090
AUS	0.002	0.034	0.24	1.31	0.25	1.63	1.1	6	0	-0.01	0.0001	0.0004
	0.008	0.046	0.67	1.82	0.74	2.26	3.03	8.24	0	-0.02	0.0002	0.0005
AMZ	-0.016	-0.054	0.26	1.46	0.3	3.04	1.62	8.57	0	0.01	0.0001	0.0008
	-0.028	-0.072	0.76	2.01	1.33	4.35	4.49	11.78	0.006	0.018	0.0004	0.001
SSA	0.004	0.064	0.21	1.16	0.06	0.43	1.19	6.35	0	-0.014	0.0001	0.0005
	0.022	0.094	0.59	1.63	0.06	0.48	3.29	8.85	-0.008	-0.024	0.0002	0.0007
CAM	-0.152	-0.424	0.16	1.28	-0.87	3.13	1.04	7.79	0	0.014	0.0001	0.0007
	-0.16	-0.412	0.74	1.95	1.76	6.85	4.4	11.52	0.008	0.026	0.0004	0.001
WNA	-0.01	0.014	0.22	1.63	-1.11	1.43	1.87	10.83	-0.018	-0.04	0.0001	0.0006
	0.01	0.042	0.9	2.41	0.92	4.29	5.73	15.15	-0.016	-0.032	0.0004	0.0008
CNA	-0.034	-0.122	0.24	1.79	-1	3.9	1.76	11.04	-0.014	-0.016	0.0001	0.0008
	-0.046	-0.126	0.99	2.69	2.64	8.98	5.8	15.58	-0.008	-0.006	0.0005	0.0012
ENA	-0.016	-0.042	0.19	1.53	-0.34	5.17	1.43	9.17	-0.02	-0.056	0.0001	0.0009
	-0.006	-0.012	0.86	2.31	3.2	9.96	4.89	13.06	-0.022	-0.052	0.0005	0.0014
ALA	0.018	0.134	0.25	1.19	0.66	0.55	1.51	8.16	-0.012	-0.02	0.0001	0.0005
	0.076	0.198	0.67	1.63	0.67	0.32	4.15	10.97	0	0.002	0.0002	0.0007
GRL	0.012	0.1	0.25	1.34	0.1	-0.41	1.61	8.49	-0.012	-0.026	0.0001	0.0005
	0.062	0.162	0.75	1.87	-0.19	-0.71	4.51	11.62	-0.002	-0.01	0.0002	0.0006
MED	-0.022	-0.086	0.2	1.72	-1.24	4.47	1.51	9.88	-0.01	-0.006	0	0.0003
	-0.046	-0.106	0.96	2.59	3.24	10.53	5.21	14.06	0	0.008	0.0002	0.0005
NEU	-0.008	0	0.19	1.22	0.38	3.03	1.39	7.86	-0.02	-0.036	0.0001	0.0005
	0.03	0.048	0.69	1.77	1.18	4.08	4.29	11	-0.012	-0.022	0.0003	0.0008
WAF	0.004	0.08	0.23	1.33	-0.19	1.01	1.83	10.55	0.002	0.032	0.0002	0.0009
	0.046	0.122	0.72	1.88	0.21	1.59	5.62	14.73	0.02	0.048	0.0005	0.0013
EAF	0.008	0.094	0.24	1.37	-0.27	0.74	1.82	10.25	0	0.014	0.0001	0.0008
	0.05	0.136	0.73	1.92	0.14	1.34	5.44	14.26	0.01	0.028	0.0004	0.0011
SAF	0	0.008	0.27	1.45	0.01	1.41	1.44	7.58	0	0.004	0.0001	0.0005
	-0.002	0.006	0.74	2	0.58	2.11	3.8	10.27	0.002	0.004	0.0002	0.0007
SAH	0.002	0.024	0.24	1.7	-2.4	-1.42	2.22	13.86	-0.006	-0.004	0.0001	0.0006
	0.012	0.04	0.96	2.54	-0.5	1.76	7.4	19.69	-0.006	-0.004	0.0003	0.0009
SEA	0	0.226	0.17	0.99	0	1.3	1.11	6.82	-0.002	0.008	0.0002	0.0009
	0.128	0.38	0.54	1.4	0.49	2	3.71	9.64	0.006	0.01	0.0005	0.0013
EAS	0.016	0.124	0.15	1.36	-0.87	2.88	1.32	8.95	-0.012	-0.034	0.0001	0.001
	0.088	0.224	0.79	2.11	1.91	6.83	4.84	12.91	-0.014	-0.034	0.0006	0.0014
SAS	-0.002	0.458	0.11	1.05	-1.31	-0.08	1.14	8.34	0	0.01	0.0001	0.001
	0.316	0.848	0.63	1.66	0.09	2.11	4.75	12.38	0.002	0.018	0.0005	0.0015
CAS	0.002	0.008	0.22	1.74	-1.72	1.67	2.04	12.22	-0.012	-0.036	0	0.0003
	0.01	0.018	0.98	2.63	1.67	6.51	6.37	17.13	-0.012	-0.036	0.0002	0.0005
TIB	0.024	0.104	0.2	1.69	-1.87	-0.59	1.79	10.79	-0.016	-0.05	0.0001	0.0005
	0.048	0.136	0.94	2.55	0.49	2.99	5.65	15.14	-0.02	-0.052	0.0003	0.0007
NAS	0.008	0.092	0.3	1.6	0.48	1.96	1.88	10.08	-0.014	-0.036	0.0001	0.0006
	0.062	0.158	0.89	2.23	0.88	2.44	5.3	13.81	-0.014	-0.026	0.0003	0.0009

Table 4. Same as Table 3, but in DJF.

| Region	Prep (mm/d)		Tbot (°C)		Fsds (W/m²)		Flds (W/m²)		Wind (m/s)		Qbot (kg/kg)	
	2050	2090	2050	2090	2050	2090	2050	2090	2050	2090	2050	2090
AUS	0.012	0.064	0.26	1.29	0.16	1.07	1.87	9.31	0	0.01	0.0001	0.0006
	0.024	0.094	0.66	1.77	0.41	1.46	4.79	12.69	0.002	0.008	0.0003	0.0008
AMZ	-0.026	-0.108	0.23	1.25	0.54	3.2	1.56	8.27	0.002	0.018	0.0002	0.0009
	-0.05	-0.12	0.66	1.73	1.49	4.3	4.4	11.33	0.008	0.02	0.0005	0.0012
SSA	0.02	0.128	0.24	1.24	0.45	2.11	1.59	8	-0.004	-0.01	0.0001	0.0006
	0.062	0.188	0.63	1.72	0.89	2.71	4	10.86	-0.004	-0.01	0.0003	0.0008
CAM	-0.006	0.092	0.21	1.29	0.04	2.35	0.9	5.81	0.004	-0.004	0.0001	0.0006
	0.03	0.15	0.74	1.89	1.49	4.09	3.29	8.47	-0.006	-0.016	0.0004	0.0009
WNA	0.012	0.094	0.26	1.52	-0.36	-0.62	1.57	8.42	0	-0.036	0.0001	0.0004
	0.05	0.138	0.88	2.24	-0.34	-0.49	4.77	12.04	-0.02	-0.05	0.0002	0.0006
CNA	0.026	0.142	0.28	1.58	-0.27	0.05	1.62	8.77	0	-0.016	0.0001	0.0005
	0.076	0.21	0.89	2.28	0.11	0.65	4.81	12.34	-0.01	-0.03	0.0002	0.0007
ENA	0.042	0.242	0.31	1.77	-0.35	-0.38	1.69	9.08	0	-0.01	0.0001	0.0005
	0.132	0.344	0.99	2.55	-0.27	-0.17	5.11	12.9	-0.004	-0.016	0.0003	0.0007
ALA	0.014	0.084	0.53	2.71	-0.25	-0.43	2.76	12.46	0.002	-0.002	0	0.0002
	0.046	0.124	1.75	4.08	-1.02	-1.29	9.19	19.65	0.002	-0.004	0.0001	0.0003
GRL	0.024	0.13	0.41	2.36	-0.24	-0.77	2.19	11.12	0.01	0.03	0	0.0002
	0.082	0.198	1.45	3.53	-0.8	-1.38	6.85	16.25	0.018	0.036	0.0001	0.0003
MED	-0.006	-0.006	0.14	1.02	0.05	1.59	0.73	4.58	-0.008	-0.042	0.0001	0.0004
	0.004	0.012	0.62	1.56	0.96	2.78	2.73	6.88	-0.02	-0.062	0.0002	0.0006
NEU	0.018	0.102	0.24	1.41	-0.34	-1.01	1.8	8.89	-0.004	-0.036	0.0001	0.0004
	0.074	0.172	0.95	2.23	-1.05	-1.8	6.27	13.94	-0.014	-0.048	0.0002	0.0006
WAF	0.006	0.044	0.25	1.4	-0.36	0.08	1.83	9.88	0.002	-0.002	0.0001	0.0005
	0.016	0.058	0.77	1.98	0.2	0.84	5.24	13.57	-0.006	-0.008	0.0003	0.0008
EAF	0.028	0.144	0.23	1.27	-0.58	-1.19	1.9	10.14	0	-0.012	0.0002	0.0008
	0.064	0.186	0.7	1.79	-0.52	-0.99	5.31	13.86	-0.008	-0.022	0.0004	0.0011
SAF	-0.004	-0.006	0.25	1.28	0.25	1.56	1.61	8.29	0.002	0.01	0.0001	0.0008
	-0.014	0.004	0.66	1.76	0.67	2.13	4.31	11.33	0.004	0.01	0.0004	0.0011
SAH	0	0.006	0.23	1.4	-0.44	0.21	1.52	8.53	0.012	0.042	0	0.0004
	0	0.01	0.8	2.05	0.35	1.23	4.6	11.95	0.016	0.05	0.0002	0.0006
SEA	0.018	0.162	0.16	0.97	-0.09	0.97	1.26	7.16	0.002	0	0.0002	0.0009
	0.078	0.234	0.55	1.39	0.52	1.73	3.91	9.98	-0.002	-0.002	0.0005	0.0012
EAS	0.018	0.11	0.25	1.45	-0.33	0.03	1.56	8.3	0.004	0.008	0.0001	0.0004
	0.052	0.154	0.83	2.12	0.06	0.62	4.59	11.73	0.002	0.004	0.0002	0.0006
SAS	0.02	0.138	0.24	1.43	-0.57	-0.27	1.88	10.24	0	-0.014	0.0001	0.0007
	0.056	0.182	0.82	2.07	0.15	0.67	5.45	14.2	-0.01	-0.024	0.0004	0.001
CAS	0.002	0.044	0.28	1.64	-0.24	0.35	1.52	8.07	-0.004	-0.02	0.0001	0.0004
	0.018	0.066	0.93	2.37	0.29	1.1	4.54	11.47	-0.012	-0.03	0.0002	0.0005
TIB	0.01	0.052	0.29	1.6	-0.26	0.42	1.69	8.68	-0.004	-0.024	0.0001	0.0003
	0.026	0.07	0.9	2.29	0.33	1.29	4.67	12.05	-0.012	-0.034	0.0002	0.0004
NAS	0.022	0.112	0.4	2.23	-0.3	-0.91	2.29	11.35	0.002	0.01	0	0.0002
	0.068	0.166	1.38	3.35	-1.04	-1.73	7.37	17.05	0.002	0.01	0.0001	0.0003
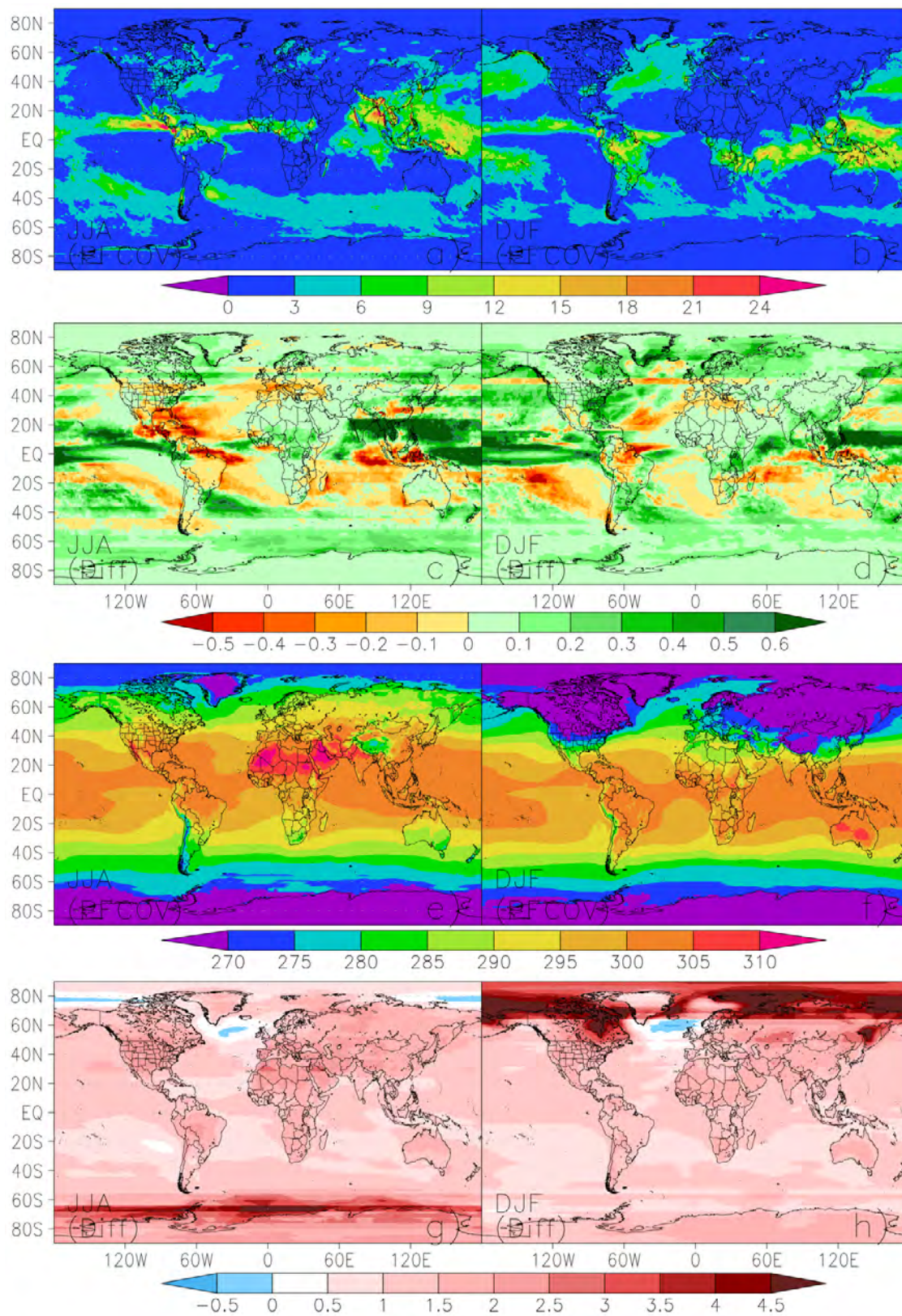
Figure 10. Ensemble medians of the precipitation (panels a-d, mm/day) and surface air temperature (panels e-h, K) in JJA (left columns) and DJF (right columns) in 2090 for the PF scenario, along with the differences (panels c, d, g, and h) from its corresponding detrended baseline counterparts in 2000.

Antarctic. The DJF temperature maxima are found in the Australian Deserts, while the minima are concentrated in the high latitude lands (North of 40°N) and Antarctic. As expected, the ensemble median air temperature is projected to increase over most of the globe relative to the detrended baseline, but its magnitudes vary regionally and seasonally (**Figure 10 g, h**). The immediately evident are the strongest JJA warming in the Antarctic Peninsula and the strongest DJF warming in the northern high latitudes (in particular the Arctic regions). Previous studies reported that the Arctic regions experience warming at twice the pace of the global average (Post *et al.* 2019; Rantanen *et al.* 2022) and unprecedented warming over the Antarctic Peninsula (González-Herrero *et al.* 2022). The general pattern of temperature increase indicates that warming is stronger over land than over oceans. The limited cooling signals are found over the northern Atlantic in both seasons as well as over the Arctic Ocean in JJA. Studies suggested that the cooling in the northern Atlantic is likely linked to the slowing of the Atlantic Meridional Overturning circulation and the resulting slower northward surface-heat transport (Caesar *et al.*, 2018; Keil *et al.*, 2020). These pattern characteristics are consistent with what were shown in Tebaldi *et al.* (2021).

5. CONCLUSIONS

We present a self-consistent, meta-ensemble, high-resolution global dataset of long-term future climate under a range of possible policy scenarios. The dataset is developed using an integrated SD-BC (delta) approach with SD for achieving the high resolution and BC for correcting the biases in the IGSM zonal climate projections. The meta-ensemble is constructed by combining the 50-member ensemble of the IGSM zonal climate projections and 18 CMIP6 climate models. The 50-member ensemble represents a range of Earth systems' response to natural and anthropogenic drivers, while the CMIP6 models characterize the uncertainty in their regional spatial response patterns as a result of forced climate warming. Our 0.5° global dataset comprises a 900-member ensemble of 9 climate variables (precipitation, mean, minimum and maximum air temperature, near-surface wind speed, shortwave and longwave radiation, specific humidity, and relative humidity) on a monthly time scale for the period 2021-2100 under four policy scenarios. Each ensemble member is packed in a single file of the self-describing netCDF format, a broadly accepted good-practice standard utilized in the weather and climate science research communities. The complete dataset is ~60 TB in size and can be made available to any interested user via public file transfer protocol. The evaluation suggests that the dataset is able to capture broadly the well-observed climate features across various regions of the globe and the results are consistent with what previous studies reported. The dataset can be used for meeting various needs associated with climate impact assessments, including uncertainty analyses, risk quantification, climate policy mitigation, and driving climate impact models which require monthly data inputs, on both global and regional scales.

6. REFERENCES

Belitz, K. & P.E. Stackelberg (2021). Evaluation of six methods for correcting bias in estimates from ensemble tree machine learning regression models. *Environmental Modelling & Software* 139, 105006

Bintanja, R. & F. Krikken (2016). Magnitude and pattern of Arctic warming governed by the seasonality of radiative forcing. *Sci Rep* **6**, 38287 (doi:10.1038/srep38287).

Broccoli, A.J., N.-C. Lau & M.J. Nath (1998). The cold ocean–warm land pattern: Model simulation and relevance to climate change detection. *J. Climate* 11, 2743–2763.

Caesar, L., S. Rahmstorf, A. Robinson, G. Feulner & V. Saba (2018). Observed fingerprint of a weakening Atlantic Ocean overturning circulation. *Nature* 556, 191–196 (doi:10.1038/s41586-018-0006-5).

Compo, G.P., J.S. Whitaker, P.D. Sardeshmukh, N. Matsui, R.J. Allan, X. Yin, B.E. Gleason, R.S. Vose, G. Rutledge, P. Bessemoulin, S. Brönnimann, M. Brunet, R.I. Crouthamel, A.N. Grant, P.Y. Groisman, P.D. Jones, M.C. Kruk, A.C. Kruger, G.J. Marshall, M. Maugeri, H.Y. Mok, Ø. Nordli, T.F. Ross, R.M. Trigo, X.L. Wang, S.D. Woodruff & S.J. Worley (2011). The Twentieth Century Reanalysis project. *Quarterly Journal of the Royal Meteorological Society* 137(654), 1– 28. (doi:10.1002/qj.776).

Ehret,U., E. Zehe, V. Wulfmeyer, K. Warrach Sagi & J. Liebert (2012). Should we apply bias correction to global and regional climate model data? *Hydrol. Earth Syst. Sci. Discuss.* **9**, 5355–5387.

Eyring, V., S. Bony, G.A. Meehl, C.A. Senior, B. Stevens, R.J. Stouffer & K.E. Taylor (2016). Overview of the Coupled Model Intercomparison Project Phase 6 (CMIP6) experimental design and organization. *Geosci. Model Dev.* 9, 1937-1958, doi:10.5194/gmd-9-1937-2016.

Giorgi, F. & R. Francisco (2000). Uncertainties in regional climate change prediction: a regional analysis of ensemble simulations with the HADCM2 coupled AOGCM. *Climate Dynamics* **16**, 169–182 (doi:10.1007/PL00013733).

González-Herrero, S., D. Barriopedro, R.M. Trigo *et al.* (2022). Climate warming amplified the 2020 record-breaking heatwave in the Antarctic Peninsula. *Commun Earth Environ* **3**, 122 (doi:10.1038/s43247-022-00450-5).

Hawkins, E., T.M. Osborne, C.K. Ho & A.J. Challinor (2013). Calibration and bias correction of climate projections for crop modelling: an idealised case study over. *Europe. Agric. For. Meteorol.* **170**, 19–31.

Jones, P. & I. Harris (2013*).* CRU TS3. 21: Climatic Research Unit (CRU) Time-Series (TS) version 3.21 of high resolution gridded data of month-by-month variation in climate (Jan. 1901–Dec. 2012). NCAS British Atmospheric Data Centre (doi:10.1002/joc.3711).

Keil, P., T. Mauritsen, J. Jungclaus, C. Hedemann, D. Olonscheck & R. Gosh (2020). Multiple drivers of the North Atlantic warming hole. *Nat. Clim. Change* 10, 667–671 (doi:10.1038/s41558-020-0819-8, 2020).

Kharin, V.V., F.W. Zwiers, X. Zhang & M. Wehner, 2013: Changes in temperature and precipitation extremes in the CMIP5 ensemble. *Climatic Change* 119, 345–357, doi:10.1007/s10584-013-0705-8.

Libardoni, A.G., C.E. Forest, A.P. Sokolov & E. Monier (2018). Estimates of climate system properties incorporating recent climate change. *Advances in Statistical Climatology, Meteorology and Oceanography* 4(1/2),19-36 (doi:10.5194/ascmo-4-19-2018).

Luo, L., A. Robock, K.Y. Vinnikov, C.A. Schlosser, A.G. Slater, N.A. Speranskaya *et al.* (2004). Effects of frozen soil on soil temperature, spring infiltration & runoff: Results from the PILPS 2(d) experiment at Valdai, Russia. *J. Hydromet,* **5**, 334-351.

Monier E *et al.* 2018 Toward a consistent modeling framework to assess multi-sectoral climate impacts *Nat. Commun.* **9** 660

O'Gorman, P.A. (2012). Sensitivity of tropical precipitation extremes to climate change. *Nat. Geosci.* 5, 697–700, doi:10.1038/ngeo1568.

O'Neill, B.C., C. Tebaldi, D.P. van Vuuren, V. Eyring, P. Friedlingstein, G. Hurtt, R. Knutti, E. Kriegler, J.-F. Lamarque, J. Lowe, G.A. Meehl, R. Moss, K. Riahi & B.M. Sanderson (2016). The Scenario Model Intercomparison Project (ScenarioMIP) for CMIP6. *Geosci. Model Dev.* 9, 3461–3482 (doi:10.5194/gmd-9-3461-2016).

Paltsev S., C.A. Schlosser, H. Chen, X. Gao, A. Gurgel, H. Jacoby, J. Morris, R. Prinn, A. Sokolov & K. Strzepek (2021). *2021 Global Change Outlook: Charting the Earth's future energy, managed resources, climate, and policy prospects*.

Post, E. *et al.* (2019). The polar regions in a 2°C warmer world. *Sci. Adv.* **5**, eaaw988.

Rantanen, M., A.Y. Karpechko, A. Lipponen *et al.* (2022). The Arctic has warmed nearly four times faster than the globe since 1979. *Commun Earth Environ* **3**(168) (doi:10.1038/s43247-022-00498-3).

Riahi, K., D. van Vuuren, E. Kriegler, J. Edmonds, B.C. O'Neill, S. Fujimori, N. Bauer, K. Calvin, R. Dellink, O. Fricko, W. Lutz, A. Popp, J.C. Cuaresma, K.C. Samir, M. Leimbach, L. Jiang, T. Kram, S. Rao, J. Emmerling, K. Ebi, T. Hasegawa, P. Havlik, F. Humpenöder, L. Aleluia Da Silva, S. Smith, E. Stehfest, V. Bosetti, J. Eom, D. Gernaat, T. Masui, J. Rogelj, J. Strefler, L. Drouet, V. Krey, G. Luderer, M. Harmsen, K. Takahashi, L. Baumstark, J.C. Doelman, M. Kainuma, Z. Klimont, G. Marangoni, H. Lotze-Campen, M. Obersteiner, A. Tabeau & M. Tavoni (2017). The Shared Socioeconomic Pathways and their energy, land use, and greenhouse gas emissions implications: An overview. *Global Environ. Chang.* doi:10.1016/j.gloenvcha.2016.05.009.

Schlosser, C.A., X. Gao, K. Strzepek, A. Sokolov, C.E. Forest, S. Awadalla & W. Farmer (2012). Quantifying the Likelihood of Regional Climate Change: A Hybridized Approach. *Journal of Climate* 26(10): 3394-3414 (doi:10.1175/ JCLI-D-11-00730.1)

Schneider, U., A. Becker, P. Finger, A. Meyer-Christoffer, M. Ziese & B. Rudolf (2014). GPCC's new land surface precipitation climatology based on quality-controlled in situ data and its role in quantifying the global water cycle. *Theoretical and Applied Climatology* 115(1-2), 15–40.

Sillmann, J., V.V. Kharin, F.W. Zwiers, X. Zhang & D. Bronaugh (2013). Climate extremes indices in the CMIP5 multimodel ensemble: Part 2. Future climate projections. *J. Geophys. Res. Atmos.* 118, 2473–2493, doi:10.1002/ jgrd.50188.

Slater, A.J., C.A. Schlosser *et al.* (2001). The representation of snow in land-surface schemes: Results from PILPS 2(d). *J. Hydromet.* **2**, 7-25.

Sokolov, A., D. Kicklighter, A. Schlosser, C. Wang, E. Monier, B. Brown-Steiner, *et al.* (2018). Description and Evaluation of the MIT Earth System Model (MESM). *Journal of Advances in Modeling Earth Systems* 10, 1759–1789 (doi:10.1002/2018MS001277).

Teutschbein, C. & J. Seibert (2012). Bias correction of regional climate model simulations for hydrological climate-change impact studies: Review and evaluation of different methods. *J. Hydrol.* 456, 12–29.

Themeßl, J.M., A. Gobiet & A. Leuprecht (2011). Empirical-statistical downscaling and error correction of daily precipitation from regional climate models. *Int. J. Climatol.* **31**, 1530–1544.

Tebaldi, C. *et al.* (2021). Climate model projections from the Scenario Model Intercomparison Project (ScenarioMIP) of CMIP6. *Earth Syst. Dynam.* 12, 253–293 (doi:10.5194/esd-12-253-2021).

Yoshimura, K. & M. Kanamitsu (2008). Dynamical global downscaling of global reanalysis. *Monthly Weather Review* 136(8), 2983–2998 (doi:10.1175/2008mwr2281.1).

Joint Program Report Series - Recent Articles

For limited quantities, Joint Program Reports are available free of charge. Contact the Joint Program Office to order.
Complete list: http://globalchange.mit.edu/publications